

## STATISTICS OF PHYSICAL PROPERTIES OF DARK MATTER CLUSTERS

Laurie D Shaw<sup>1</sup>, Jochen Weller<sup>2,3</sup>, Jeremiah P Ostriker<sup>1,4</sup>, Paul Bode<sup>4</sup>

<sup>1</sup>Institute of Astronomy, University of Cambridge, Madingley Road, Cambridge CB3 0HA, UK.

<sup>2</sup>NASA/Fermilab Astrophysics Group, Fermi National Accelerator Laboratory, Batavia, IL 60510-0500, USA.

<sup>3</sup>Department of Physics and Astronomy, University College London, Gower Street, London WC1E 6BT, UK.

<sup>4</sup>Princeton University Observatory, Princeton NJ 08544-1001, USA.

*Draft version November 15, 2018*

### ABSTRACT

We have identified over 2000 well resolved cluster halos, and also their associated bound subhalos, from the output of a  $1024^3$  particle cosmological N-body simulation (of box size  $320h^{-1}$ Mpc and softening length  $3.2h^{-1}$ kpc). This has allowed us to measure halo quantities in a statistically meaningful way, and for the first time analyse their distribution for a large and well resolved sample. We characterize each halo in terms of its morphology, concentration, spin, circular velocity and the fraction of their mass in substructure. We also identify those halos that have not yet reached a state of dynamical equilibrium using the virial theorem with an additional correction to account for the surface pressure at the boundary. These amount to 3.4% of our initial sample. For the virialized halos, we find a median of 5.6% of halo mass is contained within substructure, with the distribution ranging between no identified subhalos to 65%. The fraction of mass in substructure increases with halo mass with logarithmic slope of  $0.44 \pm 0.06$ . Halos tend to have a prolate morphology, becoming more so with increasing mass. Subhalos have a greater orbital angular momentum per unit mass than their host halo. Furthermore, their orbital angular momentum is typically well aligned with that of their host. Overall, we find that dimensionless properties of dark matter halos do depend on their mass, thereby demonstrating a lack of self-similarity.

*Subject headings:* cosmology: dark matter— galaxies: clusters: general— methods: N-body simulations

### 1. INTRODUCTION

N-body dark matter simulations have proven to be one of our most valuable tools for testing the predictions of the standard model of hierarchical structure formation. Indeed, it is largely through studying the structures that form in such simulations that we are able to investigate proposed models that describe the relative mass distribution of halos and the subhalos within them, as well as their physical characteristics such as spin, shape, and concentration.

Until the end of the last decade, it was not possible reach the required mass resolution to enable the identification of galaxy mass halos as substructures in clusters (White 1976; van Kampen 1995; Summers et al. 1995; Moore et al. 1996). Commonly known as the *overmerging* problem, this was mainly due to the limited mass and force resolution of the simulations used. The major causes of this problem were premature tidal disruption due to inadequate force resolution and two-particle evaporation for halos with a small number of particles (Klypin et al. 1999). However, rapid advances in parallel computing, through both the improvement of hardware and the development of fast and efficient parallel algorithms, has enabled us to achieve the numerical resolution required to overcome the numerical problems (Ghigna et al. 1998a; Klypin et al. 1999; Moore et al. 1999; Okamoto & Habe 1999; Ghigna et al. 2000; Springel et al. 2001; Bode et al. 2001; Kravtsov et al. 2004a; De Lucia et al. 2004; Springel et al. 2005).

There are two preferred approaches for investigating the physical properties of simulated dark matter halos. In order to achieve high numerical precision—

thus allowing the accurate identification of low mass subhalos and measurement of the properties in the innermost regions— many previous studies have adopted a resimulation technique (e.g. Navarro et al. (1995), Navarro et al. (1996), (hereafter referred to as NFW), Gao et al. (2005), Navarro et al. (2004), Moore et al. (1999), Reed et al. (2005a)). This involves extracting a halo from a cosmological simulation and resimulating it at much higher resolution, approximating the tidal field of the surrounding structures. By picking a ‘nice’ (or relaxed) halo in the original simulation, it can furthermore be ensured that the final halo will be in dynamic equilibrium. Using this technique, Diemand et al. (2005) completed the first billion particle halo simulation, achieving unprecedented resolution and probing the halo density profile to within 0.1% of the halo virial radius.

However, there are two downsides to this approach. Firstly, resimulating a small number of halos prevents an accurate determination of the *distribution* their physical properties. Previous studies have typically resimulated several halos in an attempt to ascertain if geometric and dynamical properties differ with mass. There remains a significant degree of uncertainty in the results of such studies merely because of the small number statistics involved. The resimulated halos do not present an accurate picture of the entire range of physical characteristics that may be adopted by dark matter halos when one chooses only relaxed halos for higher resolution.

The second approach that one can take is to uniformly simulate a cosmological volume at the highest resolution possible (given the available resources) and pick out a large number of halos. Although the ability to achieve higher possible mass resolution is

lost, this method results in a statistically significant sample of halos. A number of previous studies (e.g. Davis et al. (1985), Warren et al. (1992), Cole & Lacey (1996), Bullock et al. (2001b)) employed this approach to analyse the distribution of the integral properties of a large sample of halos, including their virial mass, spin and overall distribution over the volume simulated; or they used the dark matter distributions to estimate the large angle gravitational lensing of background sources (e.g. Wambsganss et al. 2004). Kravtsov et al. (2004a) performed simulations with high enough resolution to identify substructures and even subsubstructures within the cluster halos extracted from the simulation box. They analyze the halo occupation distribution for the host halos and the two-point correlation function of the galaxy size halos and subhalos, finding the results to be in good agreement with those from the Sloan Digital Sky Survey. Recently, Springel et al. (2005) presented initial results from the “*Millenium*” simulation – the highest resolution cosmological N-body simulation to date – containing  $2160^3$  particles in a cube of side length  $500h^{-1}Mpc$ . This simulation was performed using the new parallel GADGET2 code (Springel 2005) which adopts a variant of the Tree-Particle-Mesh (hereafter, TPM) technique for calculating the gravitational forces on each particle (Bode et al. 2001; Bode & Ostriker 2003).

This paper takes the second approach, presenting an analysis of a  $1024^3$  particle simulation with box size  $320 h^{-1} Mpc$  evolved using the TPM algorithm of Bode & Ostriker (2003) and containing more than 57,000 structures at the last timestep. Of these we have analysed the most massive 2200 cluster halos containing at least 10,000 particles each, thus achieving unprecedented resolution in such a large sample of halos. The clusters are first identified using a friends-of-friends algorithm; we then employ the geometrically based Denmax routine of Bertschinger & Gelb (1991) to identify the subhalos in each cluster and build family trees. Finally, all energetically unbound particles are removed. The algorithm we employ up to this stage is described in detail in Weller et al. (2005).

We first present a procedure to identify the halos that are still in the processes of formation and have not yet achieved a dynamically relaxed, virialized state. The purpose of this is to enable an independent analysis of the physical characteristics of those halos that are dynamically relaxed. A catalogue of the main physical properties of the halos is then compiled, including morphology, spin, fraction of mass in substructure, the subhalo mass function, concentration and maximum circular velocity. We analyse the distributions of each quantity, which are well defined due to the size of our sample, the dependence, if any, on halo mass, and how halo substructure influences overall cluster properties. The key questions we ask therefore, are

- What is the effect of the dynamical state of the halo on the physical properties that we measure?
- What are range the of values that the physical properties of the halos take (in the mass range we investigate)?
- Are cluster halos self-similar, i.e. how do the prop-

erties of halos vary with halo mass?

- What is the effect of substructure on the overall characteristics of a cluster?

In Section 2 we describe in detail the sample of halos that we analyse in this paper and how unvirialized clusters can be identified. In Section 3 we discuss the physical properties that we measure and how we do so. In Sections 4, 5, and 6 we present the main results of our analysis— the distribution of halo properties, how they depend on halo mass and the impact of substructure on halo properties. Finally, in Section 7 we discuss the results and state our conclusions.

## 2. DEFINITION OF SAMPLE

### 2.1. *The Identification of Halos and Subhalos*

There are many possible algorithms for defining and identifying halos and subhalos, and there is no generally agreed upon best method adopted by current investigations. Some methods are essentially geometrical and others aim at finding dynamically coherent structures; all contain both dimensionless and dimensional parameters. In general, there are three levels of refinement that one can adopt. The most basic is to use a geometrical routine such as the friends-of-friends (Huchra & Geller 1982; Davis et al. 1985; Lacey & Cole 1994) or Denmax (Bertschinger & Gelb 1991; Gelb & Bertschinger 1994; Eisenstein & Hut 1998) algorithms. These use only instantaneous particle positions to group together nearby particles (defined by the FOF ‘linking length’ or the Denmax ‘smoothing length’) into localized structures. Neither method performs any type of dynamical analysis to check whether these structures are bound.

The next level of refinement is to follow a geometrical identification of subhalos with a procedure for iteratively removing the unbound particles with the greatest total energy until only bound particles remain. Examples of routines that use this approach include SKID (Stadel et al. 1997), BDM (Klypin et al. 1999), MHF (Gill et al. 2004a) and SUBFIND (Springel et al. 2001). In each of these, the unbinding is performed assuming the subhalo is completely isolated, i.e. only the bound particles in the halo at each iteration are taken into consideration when calculating the potential energy of each particle. Not taken into account in this energy calculation are the (previously identified) unbound particles located spatially within the subhalo, nor the disruptive effect of the tidal forces from the particles surrounding it. In Shaw et al. (2006) we investigate the impact of allowing for these forces, finding there to be little difference in the subhalo populations measured; the increase in the binding energy of a subhalo from including all the particles located within it is almost entirely balanced by the losses due to the external forces.

In this paper we follow previous authors and implement only the first refinement— identifying energetically bound structures— to an initial geometrical selection of structures. The algorithm is described in detail by Weller et al. (2005) and is applied to a  $\Lambda$ CDM N-body simulation of  $1024^3$  particles with box size  $320h^{-1}Mpc$  and a spline kernel force softening length (Hernquist & Katz 1989) of  $\epsilon = 3.2h^{-1}kpc$ . This simulation was evolved to  $z=0.05$  using the Tree-Particle-Mesh

(TPM) algorithm (Bode & Ostriker 2003). The cosmological parameters used include  $\Omega_m = 0.3$ ,  $\Lambda = 0.7$ , and  $\sigma_8 = 0.95$ ; outputs from this run have previously been used to make predictions concerning strong lensing (Wambsganss et al. 2004; Hennawi et al. 2005). We wish to ensure that all the halos are well resolved and that the overmerging problem is not in evidence. Thus we discard all halos with less than 10,000 particles. The minimum halo mass allowed is therefore  $\approx 3 \times 10^{13} h^{-1} M_\odot$ .

The method described in Weller et al. (2005) starts with the hierarchical identification of structures: firstly the large clusters are identified through a Friends-of-Friends (FOF) routine with a linking length of  $b = 0.2\bar{n}^{-1/3}$ , where  $\bar{n}^{-1/3}$  is the mean inter-particle separation. The Denmax routine of Bertschinger & Gelb (1991) is then run on each FOF halo with a high resolution smoothing length of  $5\epsilon$  in order to identify the substructures within each cluster halo. A family tree is then constructed by hierarchically associating the smallest mass subhalos with their lowest mass ‘ancestor’, so that each subhalo has only a single immediate parent. Those that consist of less than 30 particles are dissolved into their immediate parent.

Up until this point the analysis is purely geometrical. Next, energetically unbound particles are discarded, first by removing the velocity outliers, and then by iteratively identifying those particles with a total energy greater than zero (in the center of mass frame of the halo) and removing the most energetic. If at any stage the mass of a subhalo drops below 30 particles, we dissolve it into its immediate parent. We then check to see if pairs of the immediate daughters of the parent cluster halo are bound. If this is the case, they form a hyperstructure: the less massive of the two becomes a daughter of the more massive structure. Finally, we remove all subhalos that are not bound to the biggest structure—the mother halo—and any particles that are not bound to the entire cluster. As described in Weller et al. (2005), this entire procedure is both stable and largely independent of arbitrary parameters choice. Henceforth, we refer to the most massive structure in each halo as the ‘mother’ or ‘host’ halo. Substructure particles are those that are also bound to any other smaller structure within the halo. We use ‘cluster’ or ‘the halo’ to refer to the entire assembly.

In this study, we also incorporate an additional step: the tagging of ‘irregular’ halos in our sample. The purpose of this is to allow a separate analysis of those halos that are still undergoing significant changes through their involvement in a major-merger. This is described in the following Section.

## 2.2. Virialization Criterion—Identifying Irregular Halos

One of the main aims of this study is to compare the physical properties of the virialized halos in our sample to those that are still in the process of forming. To achieve this we sort through the halo catalogue to isolate and tag two types of halo:

- those with mass below a certain threshold, to ensure that all the halos are well resolved and that the overmerging problem is not in evidence. These are eliminated from the sample.
- halos that we deem to have not yet reached a state of dynamical equilibrium. These are tagged so that we can analyse their physical characteristics separately.

To satisfy the first condition, we discard all halos with less than 10,000 particles, or  $\approx 3 \times 10^{13} h^{-1} M_\odot$ . We use the virial mass as our measure of halo mass. For a  $\Lambda$ CDM cosmology, it is conventional to define the virial mass  $M_{\text{vir}}$  and radius  $R_{\text{vir}}$  as  $M_{\text{vir}} = \frac{4}{3}\pi R_{\text{vir}}^3 \Delta_c(z) \rho_c(z)$ , where  $\rho_c$  is the critical density of the universe, and the mean over-density  $\Delta_c = 178\Omega_m(z)^{0.45}$  (Lahav et al. 1991). In order to calculate the virial mass of each halo, we start at its density maximum and proceed outward until we reach the virial radius, within which the mean over-density is  $\Delta_c$ . Further, we include substructures whose center of mass is within the virial radius. Hence we, define a particle as being part of the halo if it is bound to the halo and lies within the virial radius, or is part of a bound subhalo that has its center of mass within the virial radius. When quoting halo masses, we do so relative to the characteristic mass scale,  $M_* = 8.0 \times 10^{14} h^{-1} M_\odot$ , obtained by fitting a Schechter function to the mass distribution of all halos with greater than 5000 particles in the simulation box (see Figure 2 in Weller et al. (2005)). At this stage, having removed the low mass halos, we have an overall sample of 2159 halos.

For the second requirement, we use the virial theorem to determine which halos are not dynamically relaxed. The virial theorem for a system in equilibrium is usually stated as  $2T_0 + W_0 = 0$ , where  $T_0$  is the total kinetic energy of the halo, and  $W_0$  the total potential energy. However, this assumes a system with finite phase space volume, and also that each halo is in complete isolation and that all mass associated with the halo has been considered. In selecting a halo, a cut is made at some outer boundary, in this case corresponding to the isodensity contour at which the spherically averaged density is  $\Delta_c \approx 100$  times the critical density (Lahav et al. 1991). Any particles bound to the halo outside of the virial radius are by the standard convention not included when we calculate the total gravitational and kinetic energy for each halo. However, these particles do make a significant overall contribution to the pressure at the halo boundary, and so we must incorporate an additional term into the virial theorem to account for them. This correction manifests itself as a form of surface pressure at the boundary (Chandrasekhar 1961) of the halo, with the energy content

$$E_s = \int P_s(r) \mathbf{r} \cdot d\mathbf{S}. \quad (1)$$

The full and exact version of the virial theorem for a self-gravitating system is thus

$$\frac{1}{2} \frac{d^2 I}{dt^2} = 2T_0 + W_0 - E_s, \quad (2)$$

where  $I$  is the moment of inertia of the halo. We therefore define as our measure of ‘virialization’ the following:

$$\beta \equiv \frac{2T_0 - E_s}{W_0} + 1, \quad (3)$$

where  $\beta \rightarrow 0$  as  $\ddot{I} \rightarrow 0$ .

In practice, we compute  $P_s$  in the following manner: First, we rank order all the particles in the halo by radius and select the outermost 20%. We label the radius of the innermost particle in this shell as  $R_{0.8}$ , the outermost as  $R_{\text{vir}}$  and the median as  $R_{0.9}$ . Using the ideal gas law, we can approximate the surface pressure term,

$$P_s = (1/3) \frac{\sum_i (m_i v_i^2)}{V}, \quad (4)$$

summing over all particles that lie between  $R_{0.8}$  and  $R_{\text{vir}}$ .  $V$  is the volume occupied by the outermost 20%,

$$V = \frac{4\pi R_v^3}{3} - \frac{4\pi R_{0.8}^3}{3}, \quad (5)$$

hence Equation 1 can be approximated by

$$E_s \approx 4\pi R_{0.9}^3 P_s. \quad (6)$$

Figure 1 compares the virialization distribution ( $\beta$ ) of all the halos in our sample, omitting and including the surface pressure term respectively. At very low redshift, it is to be expected that the majority of the dark matter clusters in a simulation will be dynamically relaxed. By comparing these two distributions it is clear that our inclusion of the surface pressure term in the virial theorem is necessary—the distribution in the lower panel now peaks very close to zero. The tail of the distribution to negative values of  $\beta$  is largely produced by systems which are infalling and not yet virialized.

However, the virial equilibrium does not imply that  $d^2I/dt^2 = 0$  instantaneously at all times, but rather that  $\langle d^2I/dt^2 \rangle = 0$ , time-averaged over a period that is long compared to the local dynamical timescale. Therefore, we expect a roughly symmetric distribution of  $\beta \pm \sigma_\beta$  around zero due to those halos that are oscillating about the virial equilibrium position. It is difficult to know what exact value of  $\sigma_\beta$  to expect as it depends on the state of subdivision of the system. Thus, as there are also no halos with  $\beta > 0.2$ , we have picked the value of the cutoff,  $\sigma_\beta = 0.2$ , so as to leave the remaining distribution of  $\beta$  roughly symmetric about zero, as indicated by the arrow in the lower panel of Figure 1. Although this cutoff value is essentially determined arbitrarily, we feel that it sufficiently removes the particularly unvirialized halos in the tail of the distribution. Applying this criterion to our sample results in 74 (3.4%) of our halos being tagged as ‘unvirialised’. In Section 4 we demonstrate that these halos have significantly different physical properties to those that adhere to our criterium. Reducing the value of  $\sigma_\beta$  dilutes this difference, whereas increasing it does not significantly change our results.

We should also be able to apply Eq. 3 at any radii in order to determine whether the mass within is in dynamically relaxed. Figure 2 shows the variation of  $\beta$  with radius for three separate halos, including (circles) and omitting (crosses) the surface pressure correction. To create this plot, we have calculated the total kinetic potential energy for all particles within a certain fraction of the virial radius,  $r/R_{\text{vir}}$ , for spheres of successively increasing radius  $r$  out to  $R_{\text{vir}}$ . We calculate the surface pressure at each  $r$  by applying Equation 4 to the outermost 20% of particles within that radius. The three halos have been selected according to their values of  $\beta$  at  $R_{\text{vir}}$ : zero (top), 0.1 (middle) and -0.21 (bottom panel), using Equation 3. Thus the latter would be identified as

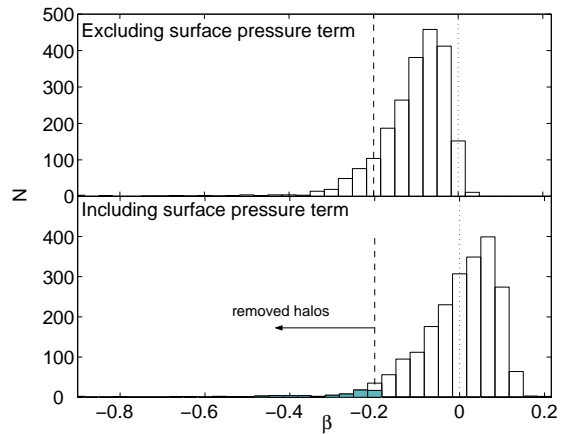


FIG. 1.— Histograms of the distribution of  $\beta$  for the halos in our sample having omitted the pressure term  $E_s$  from Equation 3 (top panel). The distribution peaks at a value just greater than -0.1, rather than at 0 as would be expected for virialized halos. Bottom panel— same as top but having included the pressure term whilst calculating  $\beta$  for each halo. The distribution now peaks much closer to zero. Also indicated (by the dashed line) is the value at which we take our lower limit of  $\beta$ . Halos with  $\beta < -0.2$  (shaded) are removed from our sample for the following analysis.

being unvirialized, according to our criterium. Density plots of the particle distributions for each of these halos can be viewed in Figures 3.

It is clear that the value of  $2T/W + 1$  (i.e.  $\beta$  omitting the surface pressure) is negative at all radii for all three halos. However, if we had been able to continue the calculations beyond the virial radius for the halos in the top two panels in Figure 2, it is likely that both would converge to zero. We note that this is found by Cole & Lacey (1996) who show in a similar plot that the ratio  $2T/|W|$  converges to unity for their halos at large radii (see their Figure 8). By neglecting to include the particles outside of the virial radius we are omitting an important term in the virial theorem required to demonstrate that these halos are in fact in dynamic equilibrium. For these two halos, the surface pressure corrections demonstrate that the correction achieved through accounting for the finite pressure and density at each radii result in values of  $\beta$  close to zero throughout. These halos appear to be uniformly in dynamical equilibrium, at all radii. The projected density plots of their particle distributions in Figure 3 (labelled *a* and *b*) suggest that they are both relaxed clusters – a massive central core with smaller orbiting substructures.

The radial distribution of  $\beta$  for the third halo (bottom panel)— also the most massive of three— is considerably more negative at each radii than the other two halos. This halo has not yet reached dynamic equilibrium; even with the surface pressure correction, which is small compared to the halo kinetic energy,  $\beta$  still remains much less than zero at all radii and appears to converge to a constant value at  $r/R_{\text{vir}} = 0.7$ . Plot *c* in Figure 3 demonstrates that this halo is clearly a complicated structure. It appears to have several clumps within its core, suggesting that it has recently undergone a major merger.

Figures 4 and 5 show how  $\beta$  varies with halo mass and with the fraction  $f_s$  of halo mass in substructure. Both of these plots also include lines representing the median

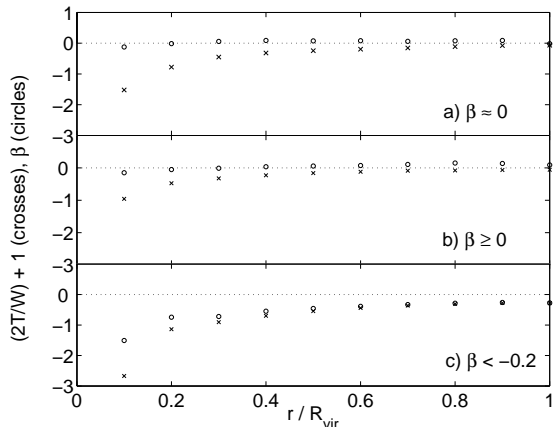


FIG. 2.— Virialization parameter  $\beta$  (Eq. 3) as a function of radius, excluding (crosses) or including (circles) the surface pressure term  $E_s$ .

values in mass and  $f_s$  bins. Only halos with  $\beta > -0.2$  have been used in calculating the trend line. From Figure 4, it appears that there is a weak trend for  $\beta$  to decrease (below zero) as halo mass increases. In accordance with the current model of hierarchical structure formation (Lacey & Cole 1993), larger and more massive objects have formed more recently through the merger of smaller structures. Hence, the most massive dark matter clusters are still in the process of dynamical relaxation and their constituent particles have an excess of kinetic energy, which we would expect to dissipate as the cluster settles into dynamic equilibrium. Halos with larger values of  $M_{vir}/M_*$  are, statistically, younger than those with smaller values of this quantity and thus are, on average, less ‘virialised’. The same explanation applies to Figure 5— which shows  $\beta$  decreasing for halos as the fraction of their mass in substructure increases— since, as we shall see, the fraction of halo mass in substructure correlates positively with  $M_{vir}/M_*$  and consequently inversely with halo age.

We will now address the objects that we intend to remove from the following analysis. These objects have abnormally high kinetic energy given their mass. They also tend to be lower mass cluster halos ( $< 10^{14} h^{-1} M_\odot$ ). In Figure 6 we plot the particle root-mean-square velocity dispersion against halo mass. We have ringed all the halos that fail the virialization cut. As expected, there is clearly a strong correlation between  $v_{rms}$  and mass for the halos we identify as virialized. The solid line represents the relationship between rms velocity dispersion and mass for an NFW profile with concentration 6.5 and  $\sigma_\theta^2(r)/\sigma_r^2(r) = 0.5$ , where  $\sigma_\theta(r)$  and  $\sigma_r(r)$  are the azimuthal and radial velocity dispersions respectively (e.g. Eq. 15 of Lokas & Mamon (2001)). We choose the above concentration as it is approximately the characteristic concentration that we obtain for our halo sample (see Sec. 5.3). Halos that failed the virial criterion clearly lie above the mass - velocity dispersion relation. As they are still in the process of relaxing into dynamical equilibrium, possibly having recently undergone a major merger, it is not surprising that they have an excess of kinetic energy.

### 3. PHYSICAL PROPERTIES OF HALOS

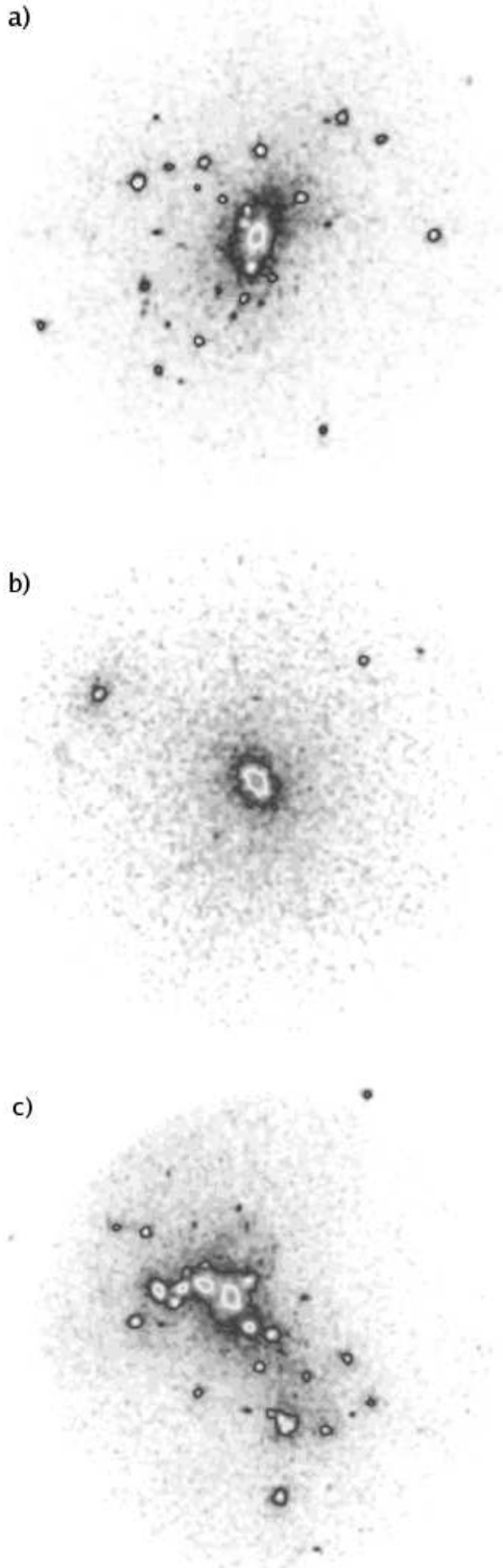


FIG. 3.— Projected density of the three example halos (labeled *a* (top), *b* (middle) and *c* (bottom)) in Figure 2.

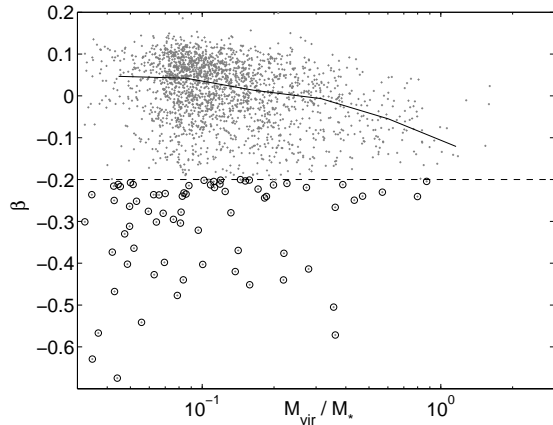


FIG. 4.— Scatter plot of  $\beta$  vs the virial mass of each halo (including the pressure term). The thick line denotes the median value of  $\beta$  in logarithmic mass bins. Halos with  $\beta < -0.2$  (circled) are not used when calculating the median values in each bin. We take  $M_* = 8.0 \times 10^{14} h^{-1} M_\odot$ .

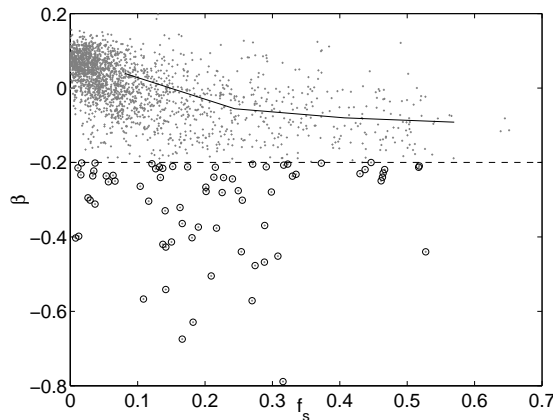


FIG. 5.— Same as Figure 4 but for  $f_s$  (the fraction of mass in substructure) rather than halo mass. The trend-line is calculated having omitted halos with  $\beta < -0.2$  (circled).

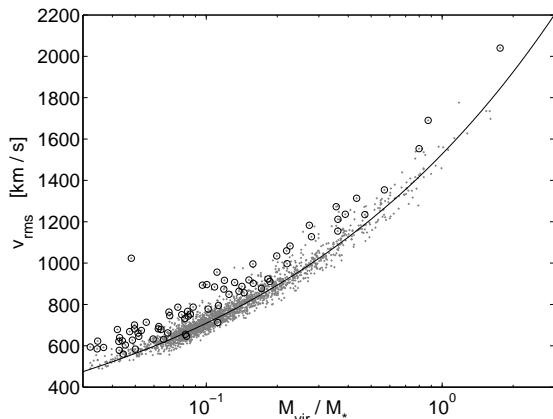


FIG. 6.— Scatter plot of halo mass,  $M_{\text{vir}}$  against the rms particle velocity in each halo. We have circled which fail the virialization cut (i.e.  $\beta < -0.2$ ). These halos depart from the otherwise strong correlation between  $v_{\text{rms}}$  and  $M_{\text{vir}}$ , appearing to have a particularly high kinetic energy per particle. The solid line is the NFW relation for mass and  $v_{\text{rms}}$ , assuming a halo concentration of 6.5.

Now that we have defined the halos included in our samples, we can proceed to discuss the physical properties that we measure. We break these down into two subsets:

- **Integral Properties.** These are properties that are obtained by summing up properties of the individual particles in each halo; halo mass, maximum circular velocity (as a measure of halo potential) and angular momentum.
- **Internal Structure.** These describe the distribution of the particles within each halo and include concentration, morphology and the distribution of substructures.

### 3.1. Integral Properties

#### 3.1.1. Maximum Circular Velocity

In order to measure the maximum circular velocity of each halo, we integrate the NFW density profile (Navarro et al. (1996) to obtain

$$V_c^2 = \frac{4\pi G r_i^3 \rho_i}{r} \left[ \ln \frac{r_i + r}{r_i} - \frac{r}{r_i + r} \right], \quad (7)$$

where  $r_i$  and  $\rho_i = 4\rho(r_i)$  are the scale radius and density, and fit to the circular velocity profile of each halo. This procedure is exploited by Klypin et al. (1999) to remove energetically unbound particles by calculating the escape velocity at the radius of each particle relative to the halo centre of mass.

The circular velocity profiles for each halo in our halo samples were measured by radially binning particles into bins of equal particle numbers. This not only ensures that the Poisson errors associated with each bin are equal, but also that the radial density of bins is proportional to the actual density of the halo at any particular radius. Using the total number of particles within the radius of the outermost particle in each bin, the circular velocity at that radius can then be calculated.

We find that the fitted parameters do not vary significantly with the number of bins used. Furthermore, binning weakens the effect of substructure on the profile parameters. To quantify the goodness of fit of the NFW for each halo, we adopt the relative standard deviation

$$\sigma_{\text{rel}} = \sqrt{\frac{\sum_{j=1}^n [(V_c(r_j) - V_{c,\text{nfw}}(r_j))/V_c(r_j)]^2}{n}}, \quad (8)$$

where  $V_c^2 = GM(< r_j)/r_j$  for bin radius  $r_j$ , and  $V_{c,\text{nfw}}(r_j)$  is the predicted NFW circular velocity at this radius. There has been much recent discussion (e.g. Klypin et al. (2001), Power et al. (2003), Hayashi et al. (2004)) regarding the conditions that must be satisfied in order to ensure numerical convergence at the innermost radius to which the circular velocity profiles are computed. Following Hayashi et al. (2004), we adopt the following three criteria:

- The number of particles enclosed within the innermost radius,  $r_{\text{in}}$ , is sufficient to ensure that five times the local collisional relaxation timescale is longer than the age of the universe, which is of the

order of the orbital timescale at the virial radius (see for example Binney & Tremaine 1987)

$$\begin{aligned} \frac{t_{relax}(r_{in})}{t_{circ}(R_{vir})} &= \frac{N(r_{in})}{8 \ln(N(r_{in}))} \frac{r_{in}/V_c(r_{in})}{r_{200}/V_{200}} \\ &= \frac{\sqrt{200}}{8} \frac{N(r_{in})}{\ln(N(r_{in}))} \left[ \frac{\bar{\rho}(r_{in})}{\rho_{crit}} \right]^{-1/2} \geq 5, \end{aligned} \quad (9)$$

where  $N(r_{in})$  is the number of particles and  $\bar{\rho}(r_{in})$  the mean density within the radius  $r_{in}$ . It takes at least 15 relaxation times for core collapse to occur and 200 for the system to evaporate, hence we have chosen 5 as a convergence criterion to allow us to probe the inner regions of each halo, without being affected by numerical instabilities.

- The innermost radius is greater than 4 softening lengths ( $\epsilon = 3.2h^{-1}kpc$  in this simulation)
- There at least 100 particles within the innermost radius

As in Hayashi et al. (2004), we find that the first constraint is the strictest for the vast majority of our halos, and virtually every halo that satisfies the third constraint automatically satisfies the second as well.

### 3.1.2. Spin

The angular momentum of simulated dark matter halos is typically been parameterized by the dimensionless spin parameter (Peebles 1969, 1980)

$$\bar{\lambda} \equiv \frac{J\sqrt{E}}{GM^{5/2}}, \quad (10)$$

where  $M$  and  $E$  are the total mass and energy of the system,  $G$  is the gravitational constant and  $J$  is the total angular momentum of the halo. This definition of spin is directly related to the ratio of the centrifugal to gravitational acceleration at the equator of a homogeneous rotating body, or the amount of angular momentum required for rotational support.

Peebles (1969) showed that the amount by which a uniformly rotating polytrope is deformed, or how oblate it is, is related to  $\lambda$  in the following way:

$$\frac{a-c}{a} \approx \frac{J^2|E|}{G^2M^5} = \bar{\lambda}^2, \quad (11)$$

i.e. the flattening of a rotating sphere is directly proportional to the square of its associated spin parameter, where  $a$  is the major and  $c$  the minor principle axis of the halo.

As we outlined in Section 1, the total energy component of  $\bar{\lambda}$  is difficult to compute due to the necessity of accounting for the surface pressure at the outer radius of each halo. This is especially the case for halos in high density regions of the simulation. Therefore, Bullock et al. (2001a) introduced an alternative parameterization,

$$\lambda = \frac{J}{\sqrt{2}MVR}, \quad (12)$$

which sidesteps this difficulty by removing the energy dependence, thus making it more practical to calculate from simulated data. We adopt this version of the spin

parameter, using the virial mass and radius for  $M$  and  $R$  respectively and calculating the circular velocity component,  $V^2 = GM(R_{vir})/R_{vir}$ . This retains some consistency between the two approaches, as  $\lambda$  reduces to  $\bar{\lambda}$  when measured at the virial radius of a truncated isothermal sphere. Hetznecker & Burkert (2005) have performed a comprehensive study of the differences between the two definitions of halo spin. In agreement with Bullock et al. (2001a) they find there to be little difference in the overall distributions of both  $\bar{\lambda}$  and  $\lambda$  at  $z=0$ . However, they also demonstrate that whilst  $\lambda$  ( $\lambda'$  in their notation) does not vary noticeably with redshift,  $\bar{\lambda}$  increases significantly as redshift decreases. This discrepancy appears to be due to the impact of the continuous acquisition of mass through accretion, which increases  $\bar{\lambda}$  but slowly decreases  $\lambda$ .

## 3.2. Internal Structure Properties

### 3.2.1. Substructure

The procedure we employ to identify substructure and build the associated family trees for each cluster halo is briefly described in Section 2. The full procedure is completely described in Weller et al. (2005). One important feature of this algorithm is that near neighbor subhalos, which are gravitationally bound to one another, are associated together. If this is not done, the subhalo distribution might depend on the geometrical smoothing lengths used in the definitions of subhalos. Here we will present the subhalo mass-function for the 2159 cluster halos in our sample, including those tagged as ‘unvirialised’.

### 3.2.2. Concentration

Halo concentration is normally defined as the ratio of some measure of the outer radius of a halo to an inner ‘scale’ radius, normally chosen to be that of the NFW profile, i.e. when the logarithmic slope of the density profile = -2. Previous studies have used various definitions of the outer radius of a halo: normally it is chosen to be the radius at which the halo density becomes some factor of the critical or mean background density of the universe at the appropriate redshift. In this study we use the virial radius to determine halo concentration, so  $c \equiv R_{vir}/r_i$ . When comparing our results with studies that have adopted an alternative definition of halo concentration (e.g. relative to the mean background, rather than the critical density) we use a conversion factor to correct for the difference.

### 3.2.3. Morphology

In order to measure halo morphology, we calculate the moment of inertia tensor for each halo,  $I_{ij} = m_p \sum_k r_k^i r_k^j$ , summed over all particles in the halo, where  $m_p$  is the particle mass in the simulation and  $r_k^i$  is the x, y or z component of the distance of the k-th particles from the cluster center of mass. We then find the magnitude and orientation of the principle axes for each halo by diagonalising  $I_{ij}$  and calculating the associated eigenvalues and eigenvectors respectively. We define the axis ratios as in Warren et al. (1992), denoting  $a$  as the longest axis,  $b$  the intermediate axis, and  $c$  the shortest axis of the moment of inertia ellipsoid.

Previous studies have calculated the inertia tensor using an iterative scheme in which only particles in

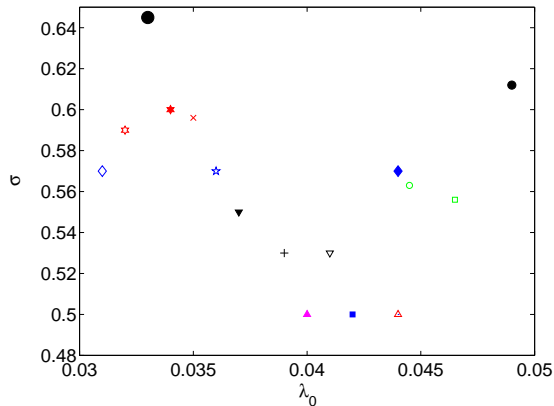


FIG. 7.— Values of  $\lambda_0$  and  $\sigma$  as in the literature (see text). The large black solid circle is the result of the analysis presented here for our main halo sample, the smaller black solid circle for our ‘unvirialised’ sample.

a particular sphere or shell are used to calculate  $I_{ij}$ . This is then repeated, using the ellipsoid or shell determined by the principle axis vectors from the diagonalized inertia tensor, until until the procedure converges (Warren et al. 1992). In agreement with Jing & Suto (2002) and Bailin & Steinmetz (2004) we find that this approach often does not converge in high resolution simulations where the over-merging problem— which tends to erase substructure in low resolution simulations— does not apply. Jing & Suto (2002) adopt a novel approach in which they fit halo shapes to isodensity contours. However, Allgood et al. (2005) find that this has the effect of suppressing the impact of large substructures near the halo core, making higher mass halos appear more prolate than they really are.

#### 4. DISTRIBUTION OF HALO PROPERTIES

In this Section we describe the distributions of the halo properties listed above for the halos in our sample. Unless specifically stated otherwise, we plot separately the properties of the halos tagged as ‘virialized’ and, where relevant, those tagged as ‘unvirialized’.

##### 4.1. Spin

As has been established in earlier studies (Barnes & Efstathiou 1987; Warren et al. 1992; van den Bosch 1998; Bullock et al. 2001a; van den Bosch et al. 2002; Gardner 2001; Vitvitska et al. 2002; Peirani et al. 2004), the distribution of  $\lambda$  is well fit by a log-normal distribution

$$P(\lambda) = \frac{1}{\lambda\sqrt{2\pi}\sigma} \exp\left(-\frac{\ln^2(\lambda/\lambda_0)}{2\sigma^2}\right). \quad (13)$$

In their analysis, Bullock et al. (2001a) find  $(\lambda_0, \sigma) = (0.042, 0.5)$  (blue, solid square in Figure 7), whilst Gardner (2001) find  $(0.044, 0.5)$  (red, upward-pointing triangle) for the halos that have undergone major mergers during their formation, and  $(0.035, 0.596)$  (red cross) for those that have grown through accretion. In a similar study, Peirani et al. (2004) found  $(0.036, 0.57)$  (blue, five-pointed star) over all the halos in their sample, whilst  $\lambda_0 \approx 0.044$  (filled blue diamond) for the merger halos and  $\lambda_0 \approx 0.031$  (blue diamond) for the accretion dominated halos (see their Figure 7). Likewise, Hetznecker & Burkert

(2005) obtain  $(0.039, 0.53)$  for their entire halo sample (black plus sign),  $(0.041, 0.53)$  for their merger halos (black, downward pointing triangle) and  $(0.037, 0.55)$  for the accretion dominated halos (filled, black downward pointing triangle). Vitvitska et al. (2002) find  $(0.0445, 0.563)$  from their numerical simulations (green circle) and  $(0.0465, 0.556)$  (green square) from their random walk model (based on the simulations). Whilst studying the dependence of  $\lambda$  on environmental density, Avila-Reese et al. (2005) obtain  $(0.032, 0.59)$  for their ‘Void’ halo sample (open, red six-pointed star) and  $(0.034, 0.60)$  for their ‘Field’ halo sample (filled, red six-pointed star). Finally, by modeling the acquisition of spin by halos from both the orbital angular momentum of merging satellites and through the effects of a large-scale tidal field (tidal torque theory— see for example Peebles 1969; White 1984), Maller et al. (2002) find that both scenarios produce a log-normal distribution of halo spin with  $\approx (0.04, 0.5)$  (filled magenta triangle). Overall, most recent studies fix  $\lambda_0$  in the range 0.031-0.045, with dispersions varying between 0.5-0.6.

The value we obtain for  $\lambda_0$  (0.033— see lower panel in Figure 8 and the large filled black solid circle in Figure 7) is in broad agreement with these studies, however we obtain a slightly broader distribution with  $\sigma = 0.645$ . For comparison, we also plot the distribution obtained by Maller et al. (2002) (dotted line in Figure 8). Interestingly, our results appear to be very similar to those obtained by Gardner (2001), Vitvitska et al. (2002) and Peirani et al. (2004) for the halos in their sample that have grown through accretion only, having not undergone any major mergers during their formation. Vitvitska et al. (2002) and Gardner (2001) both suggest that increased merging activity will result in a higher halo angular momentum— a result that is verified by Peirani et al. (2004), who monitor angular momentum as halos form in their simulations. However, the higher dispersion that we measure than any previous study does indicate that there are still a significant number of high  $\lambda_0$  halos in our sample, indeed, over 300 halos have  $\lambda_0 > 0.06$ .

The top panel in Figure 8 describes the spin distribution for halos that we have tagged as ‘unvirialized’, using the criterion outlined in Sec. 2.2. This is also well described by Eq. 13, with  $\lambda_0 = 0.049$  and  $\sigma = 0.612$  (small, black filled circle in Figure 7). A larger value of  $\lambda_0$  is consistent with the idea that these halos have not yet reached a state of dynamical equilibrium and have greater kinetic energy (partly in the form of angular momentum) than their virialized counterparts.

##### 4.2. Mass function and fraction of mass in substructure

The bottom panel in Figure 9 displays the distribution of the fraction of mass contained in substructure for our main halo sample. The median value of  $f_s$  is 0.056, where  $f_s$  ranges between  $0 \leq f_s \leq 0.65$ . Note also that there is a large tail to high values of  $f_s$ . The upper panel of Figure 9 demonstrates that the unvirialised halos do have on average more substructure, with a median value of  $f_s = 0.196$ . This indicates that these are likely to be young clusters in which there has not been sufficient time for the halo core to remove a significant fraction of subhalo mass through tidal ablation. Both Gill et al. (2004c) and De Lucia et al. (2004), who resimulate 8 and



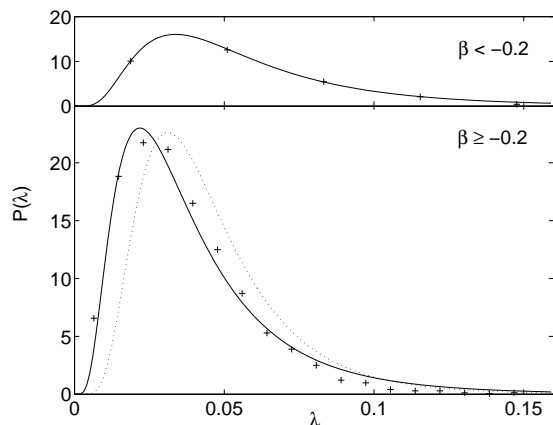


FIG. 8.— (*bottom panel*) Distribution of the halo spin parameter,  $\lambda$  (crosses) and fit of Equation 13 (solid line), where  $\lambda_0 = 0.033$  and  $\sigma = 0.645$ . For comparison, we plot a distribution with  $\lambda_0 = 0.04$  and  $\sigma = 0.5$  (Maller et al. 2002). (*top panel*) Same, but for those tagged as ‘unvirialized’, where  $\lambda_0 = 0.049$  and  $\sigma = 0.612$ .

11 cluster halos respectively, and Gao et al. (2004), who resimulate halos over a wider range of masses, obtain mean values for  $f_s$  close to the ones presented here.

In the distribution in the lower panel of Figure 9 there is tail of high  $f_s$  halos. These are halos that have very recently undergone a major merger (although they have passed our virialisation criterion) and have a dual core at their center—the mother halo and a slightly less massive subhalo. In the upper panel of Figure 10 we plot the mass of the largest subhalo as a fraction of the total mass in substructure against  $f_s$ . It is clear that, on average, halos with a large fraction of mass in substructure host a subhalo of almost equivalent mass to the mother. This is also demonstrated in the lower panel, where we plot the distance between the center of mass of the halo and its position of peak density, as a fraction of the virial radius, against  $f_s$ . The density peak, by definition, resides in the mother halo. However, for halos with an especially massive subhalo, the center of mass will lie somewhere in between the density peak of the mother and that of the subhalo. For these halos, an NFW profile provides a poor fit (see Figure 13) to the radial density profile due to the impact of the large subhalo. The correlation indicates that the center of mass moves further from the peak density position as  $f_s$  increases—suggesting that much of the substructure is clustered on one side of the halo. This can be explained if halos with large  $f_s$  are more likely to have one large piece of substructure, rather than lots of smaller subhalos that just happen to be located on one side of the mother halo.

In Figure 11 we plot the mass distribution of the subhalos we obtain from our sample of 2159 clusters, including those tagged as ‘unvirialized’. The dotted histogram is the distribution for all the sample halos, while the solid histogram only includes the 2085 virialized halos. The number density  $N_{\text{sub}}$  of subhalos of mass  $M_{\text{sub}}$  can be described by a Schechter function (Press & Schechter 1974; Schechter 1976):

$$\frac{dN_{\text{sub}}}{d\ln(M_{\text{sub}})} = N_* \left( \frac{M_{\text{sub}}}{M_{*sub}} \right)^{-\alpha} \exp \left[ -\frac{M_{\text{sub}}}{M_{*sub}} \right], \quad (14)$$

which is a power law with an exponential cut-off at large

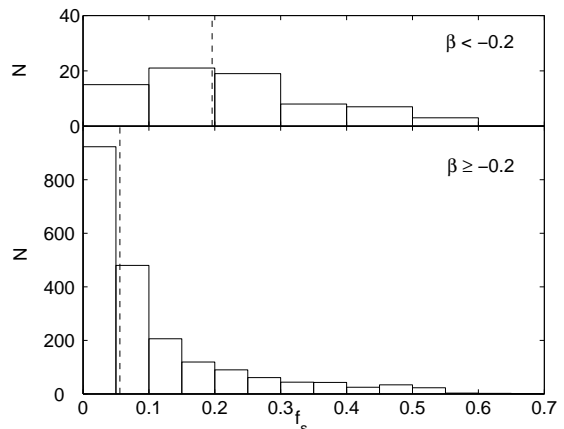


FIG. 9.— (*bottom*) Distribution of the fraction of mass in substructure for our main halo sample. (*top*) The equivalent distribution for those halos that were tagged as ‘unvirialized’

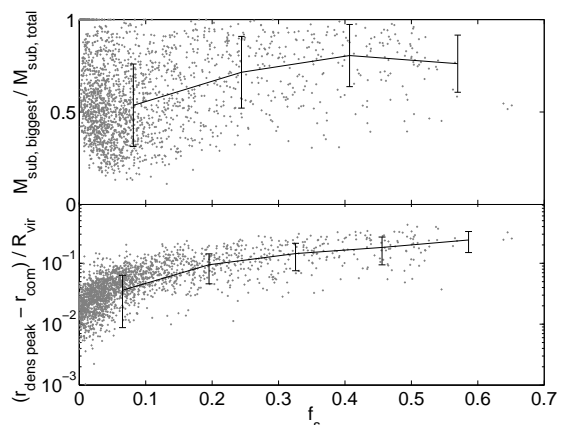


FIG. 10.— (*top*) Ratio of the mass in the most massive subhalo to the total mass in substructure, as a function of the total fraction of mass in substructure,  $f_s$ . The plot demonstrates that for halos with  $f_s > 0.3$  the substructure is largely dominated by a single massive subhalo of mass comparable to that of the mother halo. (*bottom*) Scatter plot of the distance between the point of peak density and the center of mass, as a fraction of the virial radius, for each halo against  $f_s$ .

mass scales, where  $N_*$  is a normalization constant. In Figure 11 we show the mass function of subhalos (solid line) where the substructure mass is expressed in units of the halo mass; this brings potentially different mass halos onto an equal footing. At a mass scale of about  $M_{\text{sub}} = 3 \times 10^{-3} M_h$  the function drops, because at this stage our finite sample size and the lower mass limit of our identified halos of  $7.6 \times 10^{10} h^{-1} M_\odot$  truncate the distribution.

We fit this distribution up to the truncation point with the Schechter function (Equation 14), varying all three parameters, and obtain  $\alpha = 0.5$  and  $M_{*sub} = 0.3 M_h$  (solid line). However, there are large correlations or parameter degeneracies amongst  $\alpha$ ,  $N_*$ , and  $M_{*sub}$ , which lead to marginalized errorbars in  $\alpha$  of  $\pm 0.2$  and in  $M_{*sub}$  of  $\pm 0.7 M_h$ . In order to compare with previous work we omit the cut-off,  $M_{*sub}$ , and just fit for the slope and amplitude. In this case we obtain  $\alpha = 0.75$  (dashed line). Still there is a remaining correlation between  $\alpha$  and  $N_*$  and the marginalized errorbar on the slope is  $\pm 0.12$ . If

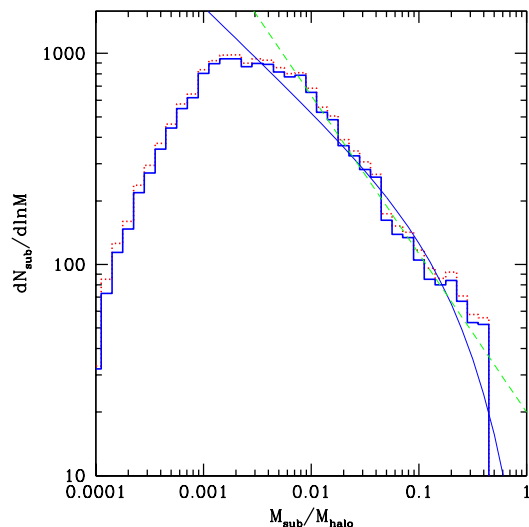


FIG. 11.— Mass distribution of subhalos from the 2159 most massive halos in our simulation as a function of the ratio of subhalo mass to cluster mass. The dotted histogram is the distribution of the complete sample, the solid histogram for the 2085 virialised halos only. The solid line is the Schechter function fits as discussed in the text. The dashed line is obtained for just fitting the slope. In both distributions halos with less than 30 particles have been dissolved into their mothers, thus setting a lower mass limit for the subhalos in our sample.

we just fit for the slope we obtain  $\alpha = 0.75 \pm 0.12$ .

Furthermore, we find the distribution becomes flat below  $M_{\text{sub}} \approx 3 \times 10^{-3} M_h$ . Others (Ghigna et al. 2000; Springel et al. 2001; De Lucia et al. 2004; Gao et al. 2004) have found similar results with regard to the power law component; but we have added an exponential cutoff at the high mass end, which is only possible of our large halo sample. We note the cutoff in high mass objects away from the simple power law, as is predicted from the Schechter prescription (Schechter 1976). Such a cutoff is of course essential, as there cannot, by definition, exist subhalos more massive than the mother halo. At this stage the distribution of subhalos is steeper than the global distribution of all the halos in our simulation (Weller et al. 2005) by almost 0.2 in the exponent. Our explanation for this is that while the original input distribution to a growing halo must correspond to the global average distribution, the more massive subhalos are more quickly destroyed as dynamical friction subjects them to more rapid tidal ablation, thus steepening the profile.

Note that the slopes of the Schechter function obtained here are lower than the ones obtained in De Lucia et al. (2004), which are in the range  $\alpha \approx 0.85 - 1.13$ . However if we fit for the slope alone the  $2\text{-}\sigma$  region of our fit is  $0.51 < \alpha < 0.99$ , which overlaps with this range of De Lucia et al. (2004). The difference between our result and previous discussions (Ghigna et al. 1998b; Moore et al. 1999; Klypin et al. 1999; Helmi et al. 2002; De Lucia et al. 2004) is due to the fact that we include *all* halos, regardless of their morphology, while previous studies picked halos which are not in merger states. While the choice of relaxed halos clearly produces a bias, our sample might be biased as well, since one expects more mergers among the most massive halos in the sim-

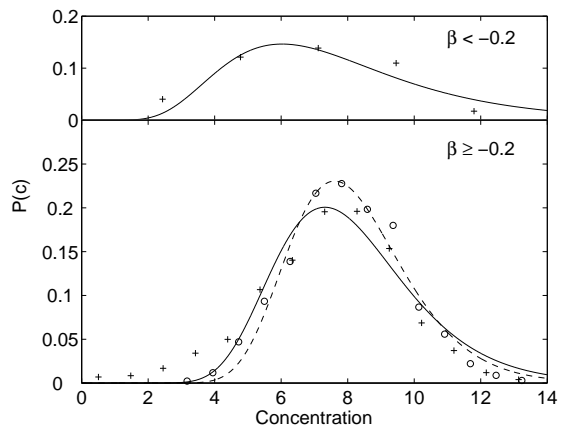


FIG. 12.— (*bottom*) Distribution of halo concentrations, including (crosses) and omitting (circles) halos with  $f_s \geq 0.3$ . Solid and dashed lines are the best fit log-normal distributions. (*top*) The distribution for halos tagged as ‘unvirialised’ according to our virialisation criterion (Sec. 2.2).

ulation than in a randomly selected sample.

#### 4.3. Concentration

It has been demonstrated by Jing (2000) and Bullock et al. (2001b) that the distribution of halo concentrations at any particular redshift can be well described by a log-normal distribution, of dispersion  $\sigma \approx 0.22$ . Dolag et al. (2004) showed that this result is independent of the adopted cosmological model. It is also thought that the dispersion in concentrations is related to the dispersion of halo formation epochs (Wechsler et al. 2002).

Figure 12 shows the best fit log-normal distribution (solid line) to our halo sample. At first glance, this Figure appears to suggest that our halo sample (crosses) does not conform to such a distribution. This is mainly due to the excess of halos with a very low concentration ( $< 3$ ). These halos appear to have significantly more mass in their outer regions than is suggested by an NFW profile. Indeed, as demonstrated in the upper panel of Figure 13, the NFW profile provides a very poor fit to these halos; the reason for this is that these halos have a considerable fraction of their mass in substructure (Figure 13, lower panel). Halos with a concentration of less than  $\sim 2.1$  are those that have a massive (bound) daughter at or near its virial radius. For these halos, the circular velocity profile continues to rise beyond  $R_{\text{vir}}$ . The open circles in Figure 12 represent the distribution of halo concentrations once all halos with  $f_s > 0.3$  are removed. It is clear that this sub-sample is well described by a log-normal distribution (dashed line) with a dispersion  $\sigma_c = 0.22$ .

The top panel displays the distribution of concentrations for the halos tagged as ‘unvirialised’. The distribution is also well described by a lognormal distribution, but peaks at a far lower concentration than the main halo sample. In these halos, much of the matter that will eventually be accreted onto the halo core is still in the outer regions, thus reducing the concentration. Furthermore, they also have (on average) a higher fraction of their mass contained within substructures, many of which are located outside the central regions of the halo.

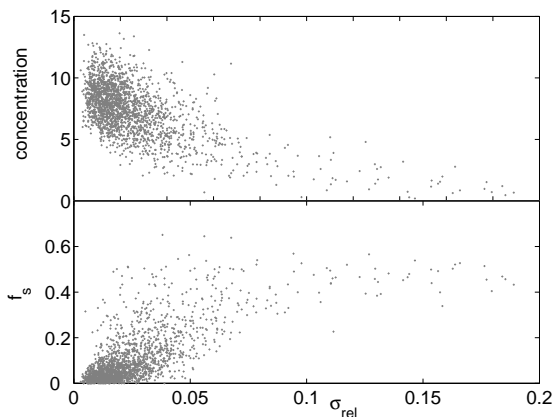


FIG. 13.— Scatter plots of halo concentration (upper panel) and the fraction of mass in substructure (lower) with respect to the goodness of the NFW profile fit (as defined by Equation 8).

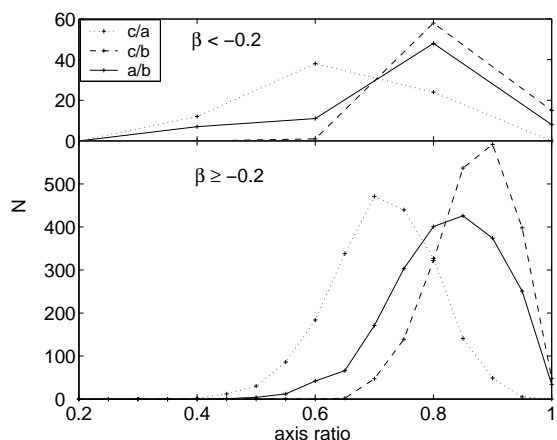


FIG. 14.— (*Bottom:*) histogram of the distributions of the halo axial ratios,  $b/a$  (solid line),  $c/b$  (dashed) and  $c/a$  (dotted). The median values agree quite well with previous studies. (*Top:*) same, but for the halos tagged as ‘unvirialised’.

#### 4.4. Morphology

Figure 14 displays the distributions for each principle axis ratio. The ratio of the intermediate to minor axes is in general greater than that of the major to intermediate axes. This implies that the halos are more prolate than oblate — a result found by several previous studies (Davis et al. 1985; Warren et al. 1992; Cole & Lacey 1996; Kasun & Evrard 2005; Bailin & Steinmetz 2004). None of the three distributions resemble a normal distribution, unlike those found by Jing & Suto (2002), who resimulate a small number of halos over a broad mass range ( $10^{12} - 10^{14} M_{\odot}$ ). As both Bailin & Steinmetz (2004) and Kasun & Evrard (2005) have found, we see a tail towards very low axis ratios, corresponding to extremely flattened halos.

The mean values we obtain for the axis ratios are  $b/a = 0.817 \pm 0.098$ ,  $c/b = 0.867 \pm 0.067$  and  $c/a = 0.707 \pm 0.095$  respectively. Again, these values agree quite well with the axis ratios found by Warren et al. (1992); Cole & Lacey (1996) and Kasun & Evrard (2005). In the case of Warren et al. (1992) we find our results match those they obtain for the largest radius used in their iterative ellipsoidal fitting technique. Dubinski & Carlberg

(1991) obtain a very low mean  $c/a$  ratio of 0.5 for the isolated collapse of halos with 100kpc radius. However, both Dubinski & Carlberg (1991) and Warren et al. (1992) also find that the halos become steadily more spherical as the length of the semi-major axis of the shell was increased in their analysis. From the Gaussian fit to their distribution of  $c/a$ , Jing & Suto (2002) find a mean value of 0.54 with a dispersion of 0.113. They then construct a conditional probability distribution for  $b/a$  over certain ranges of  $c/a$ , yielding a maximum likelihood value of 0.77 for  $b/a$ , given their mean value of  $c/a$ . Bailin & Steinmetz (2004) break each of their halos down into concentric spheres before measuring the inertia tensor in each shell (rather than for the entire halo) so it is difficult to compare directly the values we obtain for the mean axis ratios. Comparing to their most massive halos ( $10^{13} - 3 \times 10^{14} M_{\odot}$ ) we find that the axis ratios we obtain are greater (i.e. closer to 1), with the exception of those they obtain using only the innermost shells (see their Figure 3). Finally, recent results by Allgood et al. (2005) measure a  $c/a$  ratios of  $0.6 \pm 0.1$  for their galaxy mass halos. These results are also in reasonable agreement with observational work by Basilakos et al. (2000), who measure the projected cluster ellipticities of APM galaxy clusters based on moments of the smoothed galaxy distribution. They find that a prolate spheroidal model fits the data best and (without excluding clusters that show significant substructure) measure a  $c/a$  axis ratio of  $0.65 \pm 0.15$ .

Overall, the halos in our simulations are slightly more spherical than those in previous studies. This is possibly due to our selection policy of removing from our analysis subhalos that have their center of mass just outside of the virial radius of the halo. Large pieces of substructure located just outside of the halo would, if included as part of the halo, have the effect of making it appear more prolate and thus decreasing the  $c/a$  axis ratio. In order to test this we have repeated the analysis, but now including all substructure that has at least one particle inside of the virial radius of the halo. Figure 15 compares the  $c/a$  distributions obtained from this new dataset with the original. It is clear that the new histogram has many more halos with a low  $c/a$  axis ratio than the original, especially in the tail. The new mean values for the axis ratios are  $b/a = 0.79 \pm 0.121$ ,  $c/b = 0.859 \pm 0.071$  and  $c/a = 0.678 \pm 0.113$ . The fact that the mean minor-to-intermediate axis ratio has decreased the least suggests that the halos have become more prolate with the added substructure.

The top panel in Figure 14 shows the distribution of the axis ratios for the halos that we have tagged as being ‘unvirialized’ according to our criterion outlined in Sec. 2.2. They indicate that these halos are less spherical than their more relaxed counterparts, probably due to their larger fraction of mass contained in substructure. We investigate further the impact of substructure on halo morphology in Section 6.

Another way in which the shape of simulated dark matter halos can be classified is in terms of their triaxiality,  $T$  (Warren et al. 1992; Bailin & Steinmetz 2004), defined as:

$$T \equiv \frac{a^2 - b^2}{a^2 - c^2}. \quad (15)$$

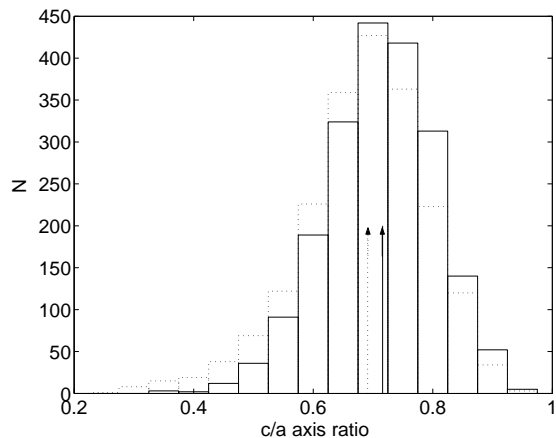


FIG. 15.— Solid histogram: distribution of the  $c/a$  axis ratio. Dotted histogram: the same, but substructure just outside of the virial radius is included in the calculation of the inertia tensor for each halo. The solid and dotted arrows indicate the median values of each distribution. There is a clear shift towards lower values of  $c/a$  when including outlying substructure, suggesting a slightly less spherical morphology.

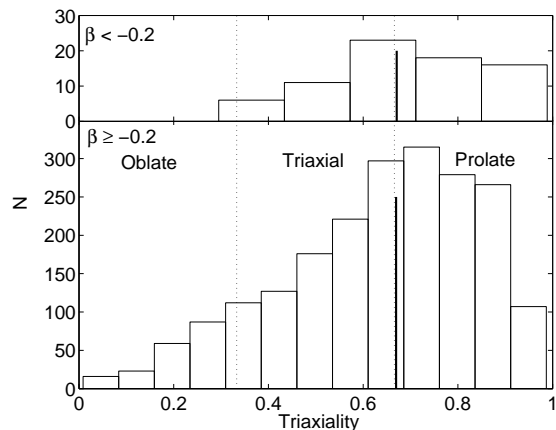


FIG. 16.— Distribution of the triaxiality,  $T$  (see Equation 15), for our main halo sample (*bottom*), and those tagged as ‘unvirialised’ (*top*). Thick black lines indicate the medians of each distribution. Both panels show that there is a clear preference for halos to adopt a more prolate, rather than oblate, morphology.

The full range of triaxiality falls into three regimes: oblate (or ‘pancake-like’) halos correspond to  $T < 1/3$ , prolate (or ‘cigar-like’) to  $T > 2/3$  and fully triaxial halos to the intermediate range. From Figure 16, it is clear that the majority (52%) of halos lie in the  $T > 2/3$  range and are therefore more prolate than oblate, with the distribution peaking at  $T \sim 0.75$ . A significant number of halos (38%) are completely triaxial — the principle axis lengths are distributed over a significant range.

## 5. CORRELATIONS WITH MASS

In this Section we investigate how the halo properties we measure correlate with halo mass. This is important for determining whether certain halo characteristics are self-similar, or whether they vary significantly depending on the age or phase of evolution of a halo. All the results presented in this Section are for the ‘virialised’ halos in our sample only. As most previous studies have found (Davis et al. 1985; Warren et al. 1992; Avila-Reese et al. 2005), we see no measurable correlation between halo

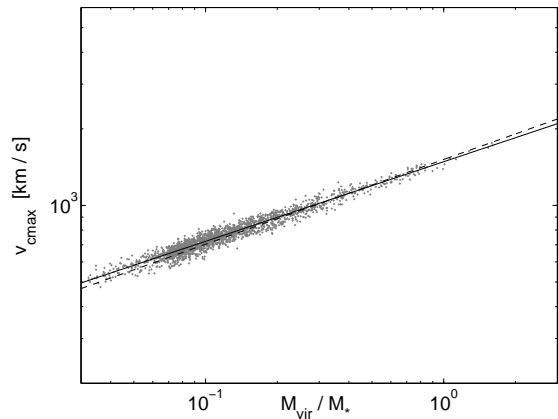


FIG. 17.— Maximum circular velocity as a function of halo mass, having removed halos for which the NFW profile provides a poor fit due to large amounts of substructure. Straight line is best fit of function  $V_{\text{cmax}} = A(M_{\text{vir}}/M_{\odot})^{\alpha}$ , with  $\alpha = 0.31 \pm 0.08$ . The dashed line is the NFW *prediction* based on our measured correlation between halo mass and concentration (Equation 16).

mass and spin.

### 5.1. Maximum Circular Velocity

Figure 17 plots maximum circular velocity as a function of virial mass. We have removed all halos with  $f_s > 0.3$  as the NFW profile provides a poor fit to many of these halos due to their large quantity of substructure (see Figure 13). Fitting a simple power-law  $V_{\text{cmax}} \propto M^{1/\alpha}$ , we measure  $\alpha = 0.31 \pm 0.08$  (solid line). This is very close to the relationship obtained by Kravtsov et al. (2004b), Bullock et al. (2001b), and Hayashi et al. (2003) (for their subhalos in the latter). Bullock et al. (2001b) explain the departure from that predicted by standard scaling of the virial parameters,  $M_{\text{vir}} \propto V_{\text{vir}}^3$ , through the observed mass dependency of the concentration parameter — a result that we also find (Section 5.3). For the NFW profile,  $V_{\text{cmax}} \propto M_{\text{vir}}^{1/3} f(c)$ , where  $f(c)$  is a function of halo concentration which in turn depends on  $M_{\text{vir}}$  (see, for example, Avila-Reese et al. (1999)). In Section 5.3 we find a power-law relation between  $c$  and  $M_{\text{vir}}$ . The dashed line in Figure 17 represents the corresponding relationship between  $M_{\text{vir}}$  and  $V_{\text{cmax}}$ .

Kravtsov et al. (2004b) follow the evolution of dwarf halos as they first accrete mass in isolation and then undergo significant mass loss through tidal stripping whilst being captured by more massive neighboring halos. They find the  $M$ - $V_{\text{cmax}}$  relationship holds throughout the differing phases of subhalo evolution. Hence, it appears that this correlation is independent of halo mass and formation epoch. This helps to explain the tightness of the relation in Figure 17.

The maximum circular velocity of a halo can be interpreted as a tracer for the depth of halo central potential. It is more reliable for this purpose than halo mass, which can be difficult to define, and especially so for subhalos. Figure 18 compares  $V_{\text{cmax}}^2$  and  $M_{\text{vir}}$  as a function of  $\phi_c$ , the gravitational potential at the point of peak density in the halo (as identified from the smoothed particle distribution by the Denmax routine in our halo finder (Weller et al. 2005)). The solid lines in each plot

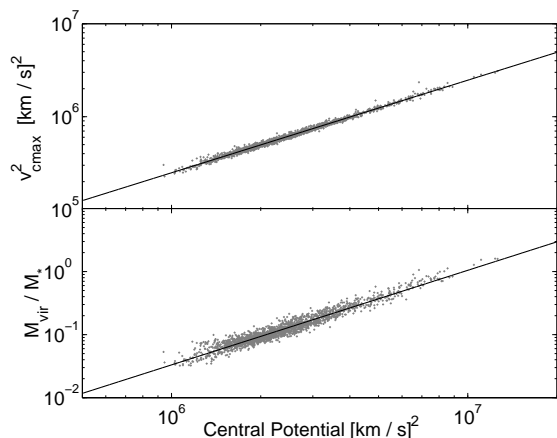


FIG. 18.— Maximum circular velocity (*top*) and halo mass (*bottom*) as a function of halo central potential,  $\phi_c$ . Lines are best fit power laws  $X \propto \phi_c^2$ , where  $X$  is  $V_{cmax}^2$  and  $\gamma = 1$  in the top panel and  $M_{vir}$  and  $\gamma = 1.5$  in the bottom.

represent the best fit power-law. We obtain  $V_{cmax}^2 \propto \phi$  in the upper panel and  $M_{vir}/M_* \propto \phi^{1.5}$  for the lower. Although both plots show clear correlations, that of  $V_{cmax}$  and  $\phi_c$  (top panel) is clearly the tighter. To quantify this, we adapt Equation 8 to measure the goodness of fit of the power-law in each case, obtaining  $\sigma_{rel} = 0.08$  for the  $V_{cmax}^2 - \phi$  correlation and  $\sigma_{rel} = 0.19$  for the mass- $\phi$  correlation. This confirms that  $V_{cmax}$  is the more robust measure of halo central potential.

### 5.2. Substructure

We plot in Figure 19 the fraction of mass in substructure as a function of halo mass. The dashed line represents the best fit power-law,  $f_s = A(M_{vir}/M_*)^m$ , with slope  $0.44 \pm 0.06$  and amplitude  $0.14 \pm 0.02$ . Hence, higher mass halos tend to have contain a higher fraction of their mass in substructure. This is an important result, demonstrating that cluster-mass halos are not self-similar. Several studies of small samples of halos selected from lower resolution simulations have suggested the dark matter halos are self-similar in terms of their subhalo populations: low mass halos appear like ‘rescaled versions’ of higher mass halos (Moore et al. 1999; Ghigna et al. 2000; De Lucia et al. 2004; Reed et al. 2005b). With a statistically significant sample of well resolved halos, we find this not to be the case. Gao et al. (2004), who compare the subhalo populations of a small sample of halos over a wide mass range, found a similar result to the one presented here. van den Bosch et al. (2005) constructed a semi-analytical model to calculate the subhalo mass function, adjusting the free parameters to match the simulations of Gao et al. (2004), Tormen et al. (2004) and De Lucia et al. (2004). They found that the slope and normalization of the mass function to be dependent on the ratio of halo mass to the characteristic non-linear mass scale. Zentner et al. (2005) and Taylor & Babul (2004) have also proposed models with similar properties, arguing that as higher mass halos have formed more recently, they should contain a higher fraction of their mass in substructure.

### 5.3. Concentration

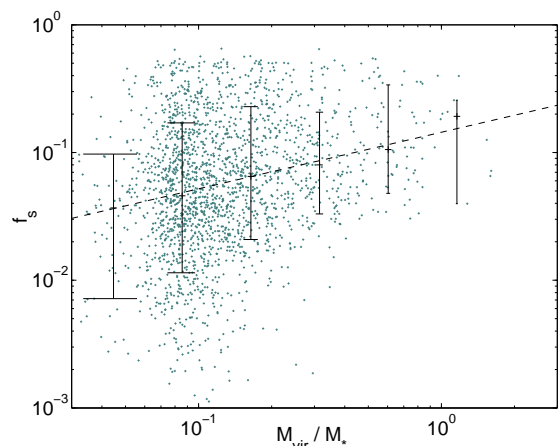


FIG. 19.— The fraction of mass in substructure as a function of halo mass. Points with errorbars represent the median values of  $f_s$  in logarithmically spaced mass bins. The dashed line is the best fit power law, with slope  $0.44 \pm 0.06$ . We take  $M_* = 8.0 \times 10^{14} h^{-1} M_\odot$ .

In their early studies, NFW postulated that the concentration of a halo is an indicator of the mean density of the universe at the time of its collapse (Navarro et al. 1997). Hence, to conform with the current paradigm of hierarchical structure formation, halo concentration ought to decrease with increasing mass. Subsequent studies (Bullock et al. 2001b; Eke et al. 2001; Dolag et al. 2004) have suggested analytic formulas predicting halo concentration as a function of mass and redshift. Dolag et al. (2004) suggest a simple fitting formula

$$c(M, z) = \frac{c_0}{1+z} \left( \frac{M}{M_*} \right)^\alpha, \quad (16)$$

finding  $\alpha = -0.102$  and  $c_0 = 5.97$  for their  $\Lambda$ CDM simulation, with  $\alpha$  almost independent of cosmology. The corresponding parameters obtained by Bullock et al. (2001b) are  $\alpha = -0.13$  and  $c_0 = 5.60$ . (It should be noted that both these studies calculate the concentration by defining the virial radius as enclosing an overdensity of  $\Delta_c$  times the *mean background* density rather than the the critical density as we do in this analysis. We therefore have applied the appropriate correction to their results to enable comparisons with our own.) Additionally, Avila-Reese et al. (2005) found a logarithmic slope of  $-0.14$  for  $c(M_{vir})$ , for the halos in high density regions in their simulations. Analysing halo concentrations at several redshifts, Bullock et al. (2001b), Eke et al. (2001) and Navarro et al. (2004) all show that the concentration parameter for a given mass is lower at higher redshifts. By following the mass accretion history of simulated halos, Zhao et al. (2003) and Tasitsiomi et al. (2004) both find that halo concentration increases during the slow accretion phase of halo formation, having remained fairly constant during an initial merger period.

The median trend (points with error bars) in Figure 20 clearly demonstrates the predicted anti-correlation between concentration and virial mass at a constant redshift for the halos in our sample. As in Section 5.1, we have removed all halos with  $f_s > 0.3$  as the NFW profile provides a poor fit to many of these halos due to their large quantity of substructure. The solid line represents the best fit for the Dolag et al. (2004) fitting formula,

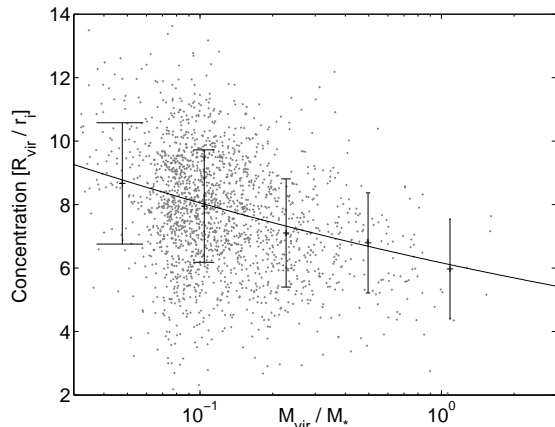


FIG. 20.— Scatter plot of concentration as a function of virial mass, having removed halos for which the NFW profile provides a poor fit due to large amounts of substructure. The points with error bars are the median concentration in logarithmic mass bins, the solid line is best fit of Eq. 16 to the data ( $\alpha = -0.12$  and  $c_0 = 6.47$ ).

with  $\alpha = -0.12 \pm 0.03$  and  $c_0 = 6.47 \pm 0.03$ . However, there is also a considerable amount of scatter in the distribution of points making it difficult to accurately determine the slope of the correlation. In their recent study, Avila-Reese et al. (2005) showed that halo concentration is also dependent on the local environmental density: halos in dense regions are on average more concentrated and have higher central densities. As demonstrated by Sheth & Tormen (2004), halos in dense regions accumulate their mass earlier than their counterparts in lower density regions. Hence, low mass halos forming in low density regions will have a lower concentration than predicted by the Dolag et al. (2004)  $M_{vir} - c$  relation. This can be seen in Figure 20— there is a significant tail of low concentration halos at lower masses.

#### 5.4. Morphology

In order to investigate how halo morphology is dependent on mass, we plot in the upper of Figure 21 the minor to major axis ratio versus halo mass. The points with error bars mark the median trend in log-linear mass bins. The solid line indicates the best fit power law,  $c/a \propto (M_{vir}/M_*)^\delta$ , with  $\delta = -0.049 \pm 0.007$ . The slope,  $\delta$ , that we obtain is in very good agreement with a comprehensive recent study of halo morphology by Allgood et al. (2005), who measure  $\delta = -0.050 \pm 0.003$  over a wide range of halo masses. In another recent paper, Paz et al. (2005) measure a steeper relationship, with  $\delta = -0.056 \pm 0.003$ . Jing & Suto (2002), who analyse a similar halo mass range to ours, find a steeper slope still. As pointed out by Allgood et al. (2005), who perform an in-depth comparison of halo morphologies from different simulations and measuring techniques, this is probably due to the approach that Jing & Suto (2002) adopt of measuring the shapes defined by isodensity contours, thus ignoring the mass distribution in the central regions of their halos. Essentially, this suppresses the effect on halo shape of large substructures near the halo core. Regardless of the shape measuring technique used, it is clear that in general halos become less spherical with mass.

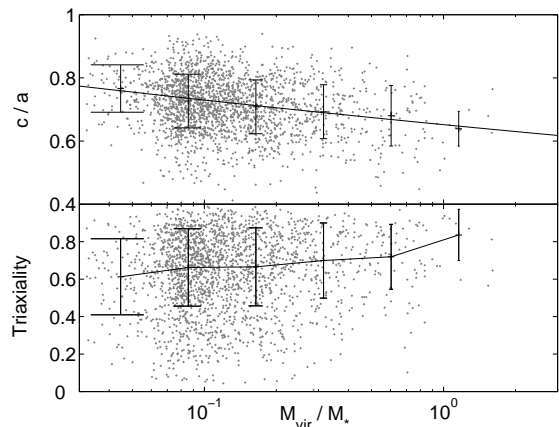


FIG. 21.— Scatter plot of halo virial mass,  $M_{vir}$ , versus the minor to major axis ratio (*top*) and halo triaxiality (*bottom*). The solid line in the top panel represents the best fit power law, with slope  $-0.049 \pm 0.007$  (see text). Points with error bars denote median value and standard deviation in log-linear mass bins. The solid line in the bottom panel is the median trend line. The plots show that higher mass halos are less spherical (decreasing  $c/a$ ) and more prolate (T approaching unity).

In the lower panel of Figure 21 we plot halo triaxiality (as defined in Equation 15) versus mass. As implied by the size of the error bars, there is an enormous amount of scatter. However, there is a preference for high mass halos to be more prolate. Therefore, the apparent trend is for dynamically ‘younger’ halos (larger  $M_{vir}/M_*$ ) to be more prolate. Low mass halos are older than their higher mass counterparts; they have had longer to dynamically relax and obtain a spherical morphology than the higher mass, more prolate halos. Furthermore, higher mass halos contain a higher fraction of their mass in substructure, which also influences their shape. This is investigated further in the following Section.

## 6. THE IMPACT OF SUBSTRUCTURE ON HALO PROPERTIES

We now investigate the impact of substructure on the physical properties of the dark matter halos. Specifically, the purpose is to determine how the distribution of subhalos effect the morphology, concentration and spin of a cluster. All the results presented in this Section are for the ‘virialised’ halos in our sample only.

### 6.1. Mass distributions and concentration

In the previous Section we found that halo concentration— an indicator of the formation epoch of a halo— decreases with halo mass. We find there to be an even tighter anti-correlation between halo concentration and the total fraction of mass in substructure: halos with more substructure have lower concentrations. This is evidence of the continuous effect of the tidal stripping of subhalos. Halos with large amounts of substructure formed more recently, when the background density of the universe— and therefore central densities and concentrations— are lower. The less dense outer parts of infalling subhalos are stripped off in the outer regions of the halo, and the denser core spirals into the central region due to dynamical friction, thus increasing the concentration of the halo once the subhalo is fully digested.

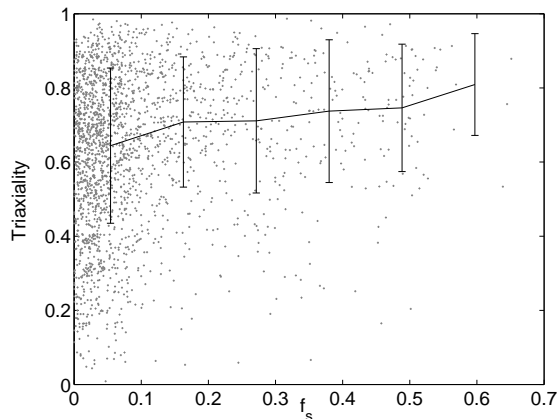


FIG. 22.— Scatter plot of the fraction of mass in substructure against halo triaxiality. Error bars represent the standard deviation in each bin. There appears to be a slight trend for triaxiality to increase with  $f_s$ , although the errors on each point are large. This indicates a tendency for halos to become more prolate as the fraction of their mass in substructure increases.

### 6.2. Contribution of substructure to halo morphology

We have already shown that substructures lying just outside of the virial radius have a measurable effect on the overall distribution for each axial ratio. Figure 22 is a scatter plot of the fraction of mass in substructure against triaxiality. Again, there is an appreciable amount of scatter, although the apparent trend is for substructure-rich halos to be more prolate. To further quantify the effect of substructure, we recalculate the  $c/a$  axis ratio for each halo, but having first removed all particles that belong to substructure, leaving particles that belong only to the ‘mother’ or ‘host’ halo. We also repeat this exercise, but removing only the most massive subhalo in the cluster and retaining the rest. Figure 23 shows the change in the minor/major axis ratio when these two sets of particles are removed. These distributions indicate that the particles belonging to the mother halo only are more spherically distributed than the rest of the halo mass. Therefore, the effect of substructure is to make cluster size halos appear more prolate. The dashed histogram demonstrates that much of the impact of substructure on the minor/major axis ratio is due to the most massive subhalo in each halo. Smaller substructures, regardless of their position in the cluster, appear to have less influence.

### 6.3. Effect of substructure on halo spin

Figure 24 shows the relation between halo angular momentum and the fraction of mass in substructure. The median value of  $\lambda$  increases from 0.030 for halos with  $f_s < 0.2$ , to 0.051 for those with  $f_s > 0.2$ . This indicates that halos with higher  $f_s$ —those more likely to have undergone major mergers—have had their angular momentum boosted through the acquisition of smaller halos.

To investigate this further, we now consider the contribution to the total spin by the mother halo only and by the substructure. To calculate these quantities we define a basic unit angular momentum per unit mass

$$[j] \equiv [2GR_{\text{vir}}M_{\text{vir}}]^{\frac{1}{2}}, \quad (17)$$

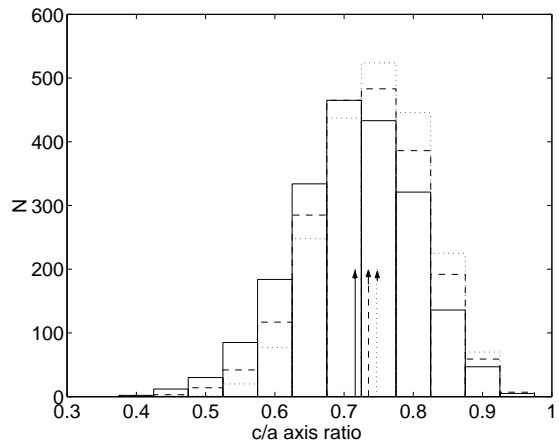


FIG. 23.— Histograms of the  $c/a$  axis ratio having included (solid) and omitted (dotted) the substructure whilst determining  $I_{ij}$  for each halo. Also plotted is the distribution having removed only the most massive subhalo (dashed). Arrows denote the median values of each distribution. The dotted histogram shows that when the substructure is discarded, thus leaving only the mother halo, the shape becomes more spherical ( $c/a$  closer to unity). It is clear that the largest subhalo is significant in determining cluster morphology: removing these results in an obvious shift in the overall  $c/a$  distribution.

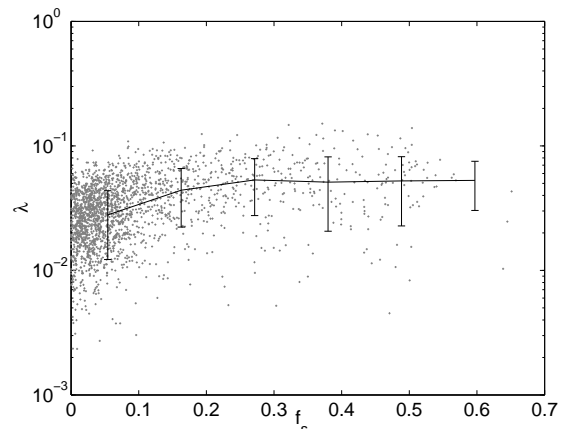


FIG. 24.— Spin parameter  $\lambda$  as a function of the fraction of mass in substructure,  $f_s$ . The median trend line shows there to be, on average, a small increase in halo spin, as the fraction of halo mass in substructure increases.

where  $R_{\text{vir}}$  and  $M_{\text{vir}}$  are the total halo energy and mass respectively. We then calculate the angular momentum per unit mass directly for particles belonging solely to the mother halo ( $\lambda_m$ ) and for those belonging to substructure ( $\lambda_s$ ) in terms of  $[j]$ :

$$\lambda_m \equiv \frac{(J_m/M_m)}{[j]}, \quad \lambda_s \equiv \frac{(J_s/M_s)}{[j]}, \quad (18)$$

where  $J_m$  and  $J_s$  are calculated using particles belonging only to the mother halo or substructure, respectively. Note if  $f_s = 0$ , then  $\lambda_s$  is also zero and  $\lambda_m$  returns to our original definition of  $\lambda$ .

Figure 25 shows the overall distributions obtained for  $\lambda_s$  and  $\lambda_m$  compared to the original distribution. We have also plotted the best fit log-normal curves (Equation 13) where  $\lambda_{0m} = 0.029$  and  $\sigma_m = 0.608$  for the mother halo, and  $\lambda_{0s} = 0.144$  and  $\sigma_s = 0.863$  for the substructure. These results clearly show that particles belonging

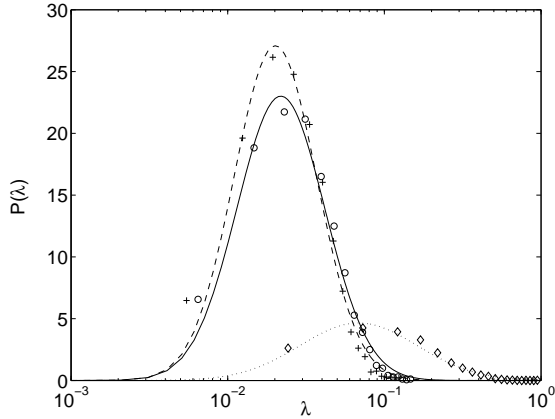


FIG. 25.— Distributions of  $\lambda$  (circles),  $\lambda_m$  (crosses) and  $\lambda_s$  (diamonds), and the respective fits to a log-normal distribution (solid, dashed, and dotted lines; see Equation 13).  $\lambda_m$  and  $\lambda_s$  are calculated using particles belonging either only to the mother halo or substructure, respectively.  $\lambda$  is plotted on a log scale due to the much greater angular momentum per unit mass (see Equation 18) of particles belonging to substructure. The fit parameters are  $\lambda_{0m} = 0.029$ ,  $\sigma_m = 0.608$  for the mother halos only, and  $\lambda_{0s} = 0.144$  and  $\sigma_s = 0.863$  for the substructure only.

to substructure have a far greater average angular momentum per unit mass than those belonging solely to the mother halo. Accreted particles will fall into a halo in a generally spherically symmetric manner, and will therefore induce only a smaller change to the total angular momentum compared to the capture of a subhalo—an injection of mass from one particular direction. Importantly, in the next Section we find that subhalos tend to be found in a prograde orbit with respect to the overall angular momentum of the mother halo, implying a preferential direction of infall. However, there is also a selection effect here. Subhalos adopting plunging orbits directly towards the cluster center of mass, and therefore possessing a lower orbital angular momentum, will be more rapidly destroyed through their exposure to tidal forces from the halo core. This introduces a bias favoring the survival of subhalos in more spherical orbits.

Overall, we expect the velocity distribution of captured dwarf halos to be fairly broad—those that form near to their eventual parents will have a lower velocity relative to the mother than those that have formed further away and have thus gained more kinetic energy as they fell into the potential well of their future host. This effect explains why  $\sigma_s$ , the dispersion in  $\lambda_s$ , is so great.

In order to investigate the effect of substructure on the spin of the mother halo, we plot  $\lambda_s$  and  $\lambda_m$  against  $f_s$  in Figure 26. In the equivalent plot for the total halo spin, we found there to be a correlation between  $\lambda$  and  $f_s$  (Figure 24). We find a similar result for the mother halo spin, but a weak anti-correlation between substructure spin and  $f_s$ . At first glance this may seem strange, but it is merely due to the fact that halos with a large  $f_s$  tend to contain at least one very massive piece of substructure. Being located near the halo center, the subhalo does not contribute as much angular momentum as several smaller and more distant subhalos would, resulting in a decreased value of  $\lambda_s$ .

The correlation between  $\lambda_m$  and  $f_s$  is a significant result. As  $\lambda_s$  decreases with increasing  $f_s$ , the overall cor-

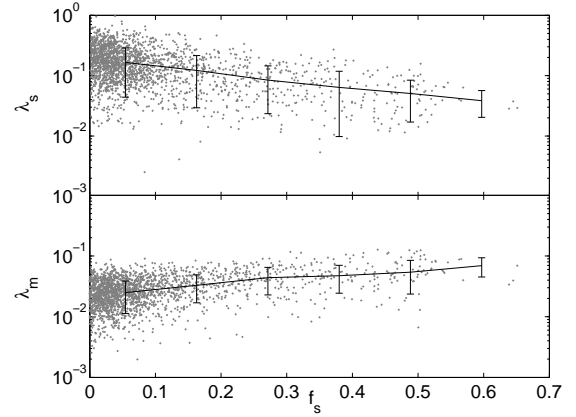


FIG. 26.— (*top*) Similar to Figure 24, except for  $\lambda$  is calculated only using particles that belong to substructure in each halo. The median trend-line shows a weak decrease of  $\lambda_s$  with  $f_s$ —the opposite to the trend demonstrated in 24, for total halo spin. (*bottom*) Same as above except for  $\lambda$  calculated only using particles that belong to the mother halo. Median trend-line shows an increase of  $\lambda_m$  with  $f_s$ . Combined, these plots demonstrate that the increase of total halo spin with  $f_s$  is due only to the increase of  $\lambda_m$  with  $f_s$ .

relation between  $\lambda$  and  $f_s$  (see Figure 24) must be entirely due to the increase in  $\lambda_m$ . We are therefore seeing evidence of the transfer of angular momentum from captured subhalos, inducing a ‘spin-up’ of the mother (we re-emphasize that the mother is that largest structure in each halo, consisting of all the particles that do not belong to any substructures). There are two possible processes by which this can occur. In the first scenario, a recently absorbed dwarf halo is slowed by gravitational dynamical friction as it penetrates into the cluster. This results in a transfer of energy and angular momentum to the surrounding particles, whilst slowing the captured halo into a more stable orbit (see Zhao (2004) for a detailed study of this process). Hence, even mother halos that host a single massive subhalo near the halo center will have a greater spin due to the transferred angular momentum as the subhalo migrates towards the center. Peirani et al. (2004) and Vitvitska et al. (2002) directly measure this effect by comparing the radial angular momentum distribution before and after a merger episode (see Figure 6 in Peirani et al. (2004)). In general they find that the maximum specific angular momentum increases sharply in the aftermath of the merger. This process is also seen indirectly by Gardner (2001) in his simulations—halos that experienced a recent merger have a larger spin than those that have grown purely through gradual accretion.

The second process by which substructure can transfer angular momentum to the host halo is through the tidal stripping of their outer regions as they orbit around the halo core. As Figure 25 shows, particles belonging to substructure have a greater angular momentum per unit mass than those that belong to the host halo. Therefore, as particles are stripped from substructure and become part of the mother halo, the mean angular momentum of the mother increases.

#### 6.4. Alignment of host and subhalo orbital angular momentum



In the preceding Section we demonstrated that clusters with a larger fraction of their mass in substructure have a greater spin. This is due to the higher average orbital angular momentum per unit mass of subhalos compared to the mother halo. However, for this to be true the majority of subhalos must have a prograde orbit with respect to the mother halo particles, i.e. the angular momentum vector for the substructure must be well aligned with that of the host. In Figure 27 we investigate this by plotting the distribution of the relative orientations of the angular momentum vectors of substructure particles ( $\mathbf{J}_s$ ), mother halo particles ( $\mathbf{J}_M$ ) and the cluster as a whole ( $\mathbf{J}_{tot} = \mathbf{J}_s + \mathbf{J}_M$ ) for each halo in our sample. The middle panel ( $\mathbf{J}_s \cdot \mathbf{J}_M$ ) is of the most interest. It clearly demonstrates that there is a tendency for  $\mathbf{J}_s$  and  $\mathbf{J}_M$  to be closely aligned. Hence, it appears that subhalos do tend to orbit in the same direction as the host halo particles.

It has been demonstrated both through observations (Plionis & Basilakos 2002) and in simulations (Colberg et al. 2005; Gill et al. 2004b; Faltenbacher et al. 2002) that subhalos preferentially fall into clusters along the filamentary structures surrounding them. Tormen (1997) and Gill et al. (2004b) both conclude that infall along filaments account for both the cluster shape and velocity structure. The correlation between the orientation of the angular momenta of mother halo and substructure particles is just a consequence of the same process responsible for the spinning up of a collapsing halo. The angular momentum of a halo is acquired through the influence of the tidal fields of neighboring structures acting on the infalling particles and subhalos during halo formation (see, for example White 1984, and references therein), the influx of which is primarily from the high density regions that eventually form filamentary structures. Once captured, the outer region of a subhalo is tidally stripped, and the dense remnant spirals into and is eventually consumed by the halo core. Thus, the mother accumulates all the orbital angular momentum of the subhalo. Over time, as subhalos are captured and absorbed, the the spin of the mother halo gradually increases in this manner. Hence, the measured alignment between the angular momentum of the mother halo and subhalo particles is merely due to the temporal auto-correlation of the angular momenta of matter accumulated by the cluster.

Additionally, a smaller halo on a prograde orbit around a cluster will gravitationally perturb nearby particles within the virial radius, causing a slight extension of the halo shape towards it (Tremaine & Weinberg 1984). This in turn increases the attraction of the cluster on the halo, thus improving the likelihood that it will be captured. Halos that pass the cluster in retrograde orbits will not be able to perturb the cluster to as great an effect. Hence, there is a slightly greater capture probability for a halo that has a lower *relative* velocity to the local cluster particles, whether it arrives from a filament or not.

### 6.5. Alignment of angular momentum and halo axes

For a rotating body, it is expected that the direction of the angular momentum vector  $\mathbf{J}$  will align with one of the principle axis vectors. The most stable configuration is when  $\mathbf{J}$  is parallel to the minor axis  $\mathbf{c}$ . Fig-

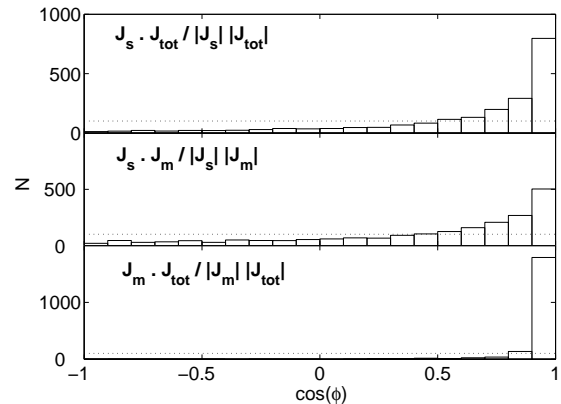


FIG. 27.— Distributions of the relative orientation of the angular momentum vectors for the entire cluster and the substructure (top panel), the substructure and the mother halo (middle panel) and the mother halo and entire cluster (bottom panel). The middle plot demonstrates that there is reasonably good alignment (to within  $25^\circ$ ) of the angular momentum of the mother halo and subhalos.

ure 28 displays the distribution of the cosine of the angle  $\phi$  between the angular momentum vector and the major, intermediate and minor axes for all the halos in our sample. There is clearly a tendency for the angular momentum vector to be aligned with the minor axis of the halos. Correspondingly, the major axis is far more likely to be nearly perpendicular to  $\mathbf{J}$ . This result was also found by Barnes & Efstathiou (1987), Warren et al. (1992), Bailin & Steinmetz (2004), Allgood et al. (2005) and Avila-Reese et al. (2005).

The intermediate axis alignment is interesting: it appears to show no preferred alignment with  $\mathbf{J}$ , having an almost uniform distribution over all  $\cos\phi$ . We have investigated whether this may be due to the difficulties in determining the minor axis when  $c/b$  is close to unity. However, we found this not to be the case—the axis ratios are widely distributed for these halos. Hence, a minority of halos are aligned so that their intermediate axes is parallel to the direction of the angular momentum vector—an unstable configuration for a solid rotating body. In Figure 29 we break down the range of  $\lambda$  into four equally sized sets. The purpose of this is to investigate whether the oddly aligned halos are those with the least (normalized) angular momentum. It is clear that as  $\lambda$  decreases the distribution of orientations becomes more evenly spread. Therefore, the orientation of a halo is therefore dependant on the magnitude of its spin. The greater the angular momentum of a halo, the more likely it is to be found rotating around the minor principle axis, and the less likely around the major axis. Except for the most rapidly rotating halos, which maintain the expected orientation, the results for the intermediate axis are inconclusive. The seemingly random distribution of alignments is maintained for slowly rotating halos.

### 6.6. Correlation between $\lambda$ and triaxiality

We now consider whether the Peebles (1969) relation between the ratio of the major and minor principle axes and the cluster spin (Equation 11) holds for the dark matter halos in our simulation. As we determined in Section 4.4, most of the halos tend to be prolate rather than oblate. Here we investigate whether there is an

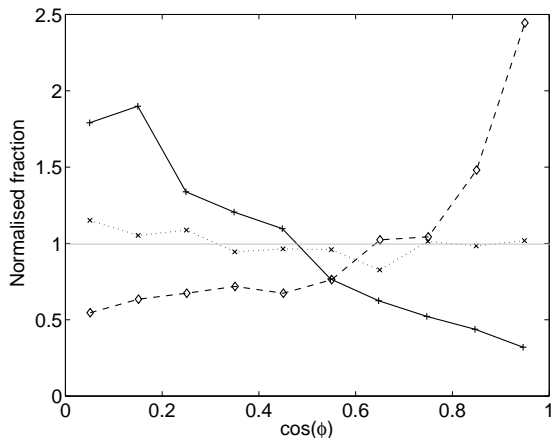


FIG. 28.— Distribution of the cosine of the angle  $\phi$  between the angular momentum vector and the major (solid), intermediate (dotted) and minor (dashed) axes. The plot is normalized so that a uniform distribution would have value of unity on the vertical axis (grayed horizontal line).

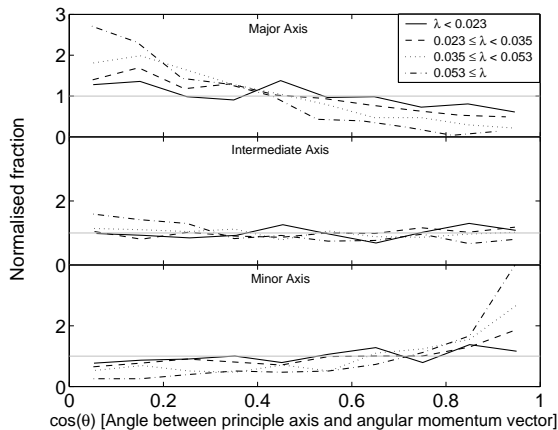


FIG. 29.— The distribution of the cosine of the angle between the angular momentum vector and the major (top panel), intermediate (middle), and minor (bottom) axis for halos grouped into ranges of total halo spin,  $\lambda$ . The plot demonstrates an improvement in alignment as  $\lambda$  increases. Rapidly spinning halos have a tendency for  $\mathbf{J}$  to be more closely aligned with the minor axis. Each plot is normalized so that a uniform distribution would have value of unity on the vertical axis (grayed horizontal lines).

increased departure from a spherical morphology (i.e. a reduction of the axis ratio  $c/a$ ) as  $\lambda$  increases.

There are at least two effects that could influence this correlation. The first of these is the possibility of a significant misalignment between the minor principle axis and the angular momentum vector. Equation 11 assumes that the object is rotating around its minor principle axis. In those halos for which there is a significant misalignment between the minor axis and the angular momentum vector, the effect of halo spin on shape will be unpredictable. However, as many of the halos in our sample are prolate, with a mean  $c/b$  axis ratio near 0.9, we include only those halos for which the angle between the major axis and the angular momentum vector is greater than or equal to  $70^\circ$ . A second possible source of uncertainty will be the effects of substructure on the halo shape. Figure 23 showed the principle axis ratios using particles belonging only to the mother halo (i.e. having

removed the subhalos) finding it to be more spherical than the entire halo. Equation 11 applies to a cylindrically symmetric and uniformly rotating polytrope, and therefore will certainly not hold when there is significant substructure in the cluster halo. Hence we discard all particles belonging to substructure before calculating the  $c/a$  axis ratio for each halo, and we use  $\lambda_m$ —the spin calculated using the mother halo particles only—rather than  $\lambda$ .

Even having accounted for these possible sources of discrepancy, we find that there is no correlation between the spin and the overall shape of the halos. It is therefore clear that other processes are responsible for determining halo morphology. The mean value we obtain for  $\lambda_0$  is 0.033. Therefore, cluster mass halos cannot support themselves through rotation alone, it is instead through their velocity dispersion that they are able to do so. Hence, spin is largely irrelevant in determining shape even though we find a strong correlation between the angular momentum vector and the minor principle axis. We have also shown that the angular momentum of dark matter halos is increased as subhalos are accumulated, which also influences halo shape. Furthermore, subhalos tend to be found in prograde orbits, partly because of a preferential direction of infall from filaments surround the halo. It appears that the orientation of dark matter clusters can be explained by the specific merging directions of smaller halos that they capture, during their formative years.

## 7. DISCUSSION AND CONCLUSION

In this study, we set out to investigate the overall physical characteristics of a sample of over 2000 massive dark matter cluster halos identified in a  $320 h^{-1}\text{Mpc}$ ,  $1024^3$  particle simulation. Using the algorithm described in Weller et al. (2005), all particles belonging to substructure in each cluster were identified, down to a minimum subhalo mass of 30 particles, or  $\sim 10^{11} h^{-1} M_\odot$ . We then applied two further criteria to our sample. First, to ensure that all the halos in our dataset were well resolved—thus ensuring that no substructure has been washed out by the so-called ‘over-merging’ problem—we set a minimum cluster halo mass of 10,000 particles, leaving us with an overall sample of 2159 halos. Second, we identified and tagged those halos not yet in a state of dynamical equilibrium. The aim of the second criterion is to enable separate analyses of those halos that are virialized and those that are still at an earlier stage of their formation.

In order to implement this second criterion, we defined a measure of virialization,  $\beta$  (Equation 3), based on the virial theorem and including a necessary term to compensate for the surface pressure at the virial radius of each halo. Using this technique, we demonstrated quantitatively that higher mass, substructure-rich halos are less virialized. We removed from our sample any halo with  $\beta < -0.2$  (i.e. those still collapsing) – which make up roughly 3.4% of the entire sample – tagging them as ‘unvirialized’. In total, our sample contained 2085 virialized halos, each containing between 10,000 and 500,000 particles. Such a large number of well resolved halos allowed us to determine their physical properties in a statistically significant way.

We then constructed a catalogue of their physical properties, including concentration, morphology, angular mo-

momentum, maximum circular velocity, and the fraction of mass in substructures. The main questions motivating our analysis were: how are the halo properties distributed, both in our main halo sample and in those that we have tagged as ‘unvirialized’? Do halo properties depend on mass? And how are they influenced by substructure? These questions can only be answered if one analyses a sample of considerable size with no prior selection of specific halos to resimulate from a lower resolution simulation. The distributions obtained in this work are drawn from a large enough sample ( $\approx 2000$ ) to address these questions in a statistical meaningful way.

The halos in our virialized sample contained a median value of 5.6% of their mass in substructure, with a tail to large substructure fractions. On average, they tended to have a prolate morphology and a mean minor to major principle axis ratio of  $c/a = 0.707 \pm 0.095$ . The unvirialized halos were more substructure-rich, with a median value of 19.6% of their mass in substructure. They also tended to be less spherical, have a higher spin and a lower concentration than their dynamically relaxed counterparts.

We have clearly demonstrated that the physical properties of halos are dependant on their mass and therefore their age. The median fraction of mass contained in substructure increases with halo mass as  $f_s \propto (M_{\text{vir}}/M_*)^m$ , where  $m = 0.44 \pm 0.06$ . This supports the prediction made by Zentner et al. (2005) that as higher mass halos have formed more recently than lower mass halos, they should contain more substructure as they have had less time to disrupt their internal subhalo population. One direct consequence of this is that higher mass halos appear more prolate: we find  $c/a \propto (M_{\text{vir}}/M_*)^\delta$ , where  $\delta = -0.049 \pm 0.007$ . As expected, halo concentration decreases as mass increases, with  $c(M) \propto (M/M_*)^\alpha$  with  $\alpha = -0.12 \pm 0.03$ , agreeing well with the slopes measured by Dolag et al. (2004) and Bullock et al. (2001b).

Halos with greater amounts of substructure tend also to have a higher spin; the angular momentum per unit

mass of subhalos is far greater than that of the mother halo. We also find evidence of the transfer of angular momentum to the mother halo (which consists of all the particles in the halo that do not belong to substructures) from captured subhalos, via dynamical friction and the tidal stripping of their outer regions. Furthermore, the orbital angular momentum of subhalos is typically well aligned with that of their host. We propose that this is mainly due to the process by which a halo accumulates angular momentum from captured subhalos, which, due to large-scale tidal fields, have a preferential direction of infall from the surrounding filaments (see, for example Colberg et al. 2005). The angular momentum of consumed subhalos is added to that of the mother halo, so that over time it will begin to rotate in the same direction to which the subhalos are ‘injected’, explaining the observed alignment. Additionally, we find that the orientation of the angular momentum vector of halo with respect its morphology is dependant its magnitude. Rapidly spinning halos tend to align with the minor principle axis; halos with very low values of  $\lambda$  are have a higher probability of being aligned with the intermediate or major axes. However, angular momentum is not responsible for determining halo shape. Indeed, we concluded that the correlation between angular momentum and the minor principle axis is due to a common influence on both properties—the preferential merging direction of subhalos along halo filaments.

JW was supported by the DOE and the NASA grant NAG 5-10842 at Fermilab. This work was supported by a grant of supercomputing time (grant number MCA04N002P) from the National Center for Supercomputing Applications. This research also used computational facilities supported by NSF grant AST-0216105. LS thanks Antonio Vale for helpful discussions and PPARC for financial support.

## REFERENCES

- Allgood, B., Flores, R. A., Primack, J. R., Kravtsov, A. V., Wechsler, R. H., Faltenbacher, A., & Bullock, J. S. 2005, astro-ph/0508497
- Avila-Reese, V., Colin, P., Gottloeber, S., Firmani, C., & Maulbetsch, C. 2005, astro-ph/0508053
- Avila-Reese, V., Firmani, C., Klypin, A., & Kravtsov, A. V. 1999, MNRAS, 310, 527
- Bailin, J. & Steinmetz, M. 2004, astro-ph/0408163
- Barnes, J. & Efstathiou, G. 1987, ApJ, 319, 575
- Basilakos, S., Plionis, M., & Maddox, S. J. 2000, MNRAS, 316, 779
- Bertschinger, E. & Gelb, J. M. 1991, Computers in Physics, 5, 164
- Binney, J. & Tremaine, S. 1987, Galactic dynamics (Princeton, NJ, Princeton University Press, 1987, 747 p.)
- Bode, P., Ostriker, J., & Turok, N. 2001, ApJ, 556, 93
- Bode, P. & Ostriker, J. P. 2003, ApJS, 145, 1B
- Bullock, J. S., Dekel, A., Kolatt, T. S., Kravtsov, A. V., Klypin, A. A., Porciani, C., & Primack, J. R. 2001a, ApJ, 555, 240
- Bullock, J. S., Kolatt, T. S., Sigad, Y., Somerville, R. S., Kravtsov, A. V., Klypin, A. A., Primack, J. R., & Dekel, A. 2001b, MNRAS, 321, 559
- Chandrasekhar, S. 1961, Hydrodynamic and Hydromagnetic Stability (Oxford University Press, Amen House, London, UK)
- Colberg, J. M., Krughoff, K. S., & Connolly, A. J. 2005, MNRAS, 275
- Cole, S. & Lacey, C. 1996, MNRAS, 281, 716
- Davis, M., Efstathiou, G., Frenk, C. S., & White, S. D. M. 1985, ApJ, 292, 371
- De Lucia, G., Kauffmann, G., Springel, V., White, S. D. M., Lanzoni, B., Stoehr, F., Tormen, G., & Yoshida, N. 2004, MNRAS, 348, 333
- Diemand, J., Zemp, M., Moore, B., Stadel, J., & Carollo, M. 2005, astro-ph/0504215
- Dolag, K., Bartelmann, M., Perrotta, F., Baccigalupi, C., Moscardini, L., Meneghetti, M., & Tormen, G. 2004, A&A, 416, 853
- Dubinski, J. & Carlberg, R. G. 1991, ApJ, 378, 496
- Eisenstein, D. J. & Hut, P. 1998, ApJ, 498, 137
- Eke, V. R., Navarro, J. F., & Steinmetz, M. 2001, ApJ, 554, 114
- Faltenbacher, A., Gottlöber, S., Kerscher, M., & Müller, V. 2002, A&A, 395, 1
- Gao, L., White, S. D. M., Jenkins, A., Frenk, C. S., & Springel, V. 2005, MNRAS, 353, 853
- Gao, L., White, S. D. M., Jenkins, A., Stoehr, F., & Springel, V. 2004, MNRAS, 355, 819
- Gardner, J. P. 2001, ApJ, 557, 616
- Gelb, J. M. & Bertschinger, E. 1994, ApJ, 436, 467
- Ghigna, S., Moore, B., Governato, F., Lake, G., Quinn, T., & Stadel, J. 1998a, MNRAS, 300, 146
- . 1998b, MNRAS, 300, 146
- . 2000, ApJ, 544, 616
- Ghigna, S. et al. 2000, ApJ, 544, 616
- Gill, S. P. D., Knebe, A., & Gibson, B. K. 2004a, MNRAS, 351, 399
- . 2004b, MNRAS, 351, 399

- Gill, S. P. D., Knebe, A., Gibson, B. K., & Dopita, M. A. 2004c, *MNRAS*, 351, 410
- Hayashi, E., Navarro, J. F., Power, C., Jenkins, A., Frenk, C. S., White, S. D. M., Springel, V., Stadel, J., & Quinn, T. R. 2004, *MNRAS*, 355, 794
- Hayashi, E., Navarro, J. F., Taylor, J. E., Stadel, J., & Quinn, T. 2003, *ApJ*, 584, 541
- Helmi, A., White, S. D., & Springel, V. 2002, *Phys. Rev. D*, 66, 063502
- Hennawi, J. F., Dalal, N., Bode, P., & Ostriker, J. P. 2005, *astro-ph/0506171*
- Hernquist, L. & Katz, N. 1989, *ApJS*, 70, 419
- Hetznecker, H. & Burkert, A. 2005, *ArXiv Astrophysics e-prints*
- Hopkins, P. F., Bahcall, N. A., & Bode, P. 2005, *ApJ*, 618, 1
- Huchra, J. P. & Geller, M. J. 1982, *ApJ*, 257, 423
- Jing, Y. P. 2000, *ApJ*, 535, 30
- Jing, Y. P. & Suto, Y. 2002, *ApJ*, 574, 538
- Kasun, S. F. & Evrard, A. E. 2005, *ApJ*, 629, 781
- Klypin, A., Gottlöber, S., Kravtsov, A. V., & Khokhlov, A. M. 1999, *ApJ*, 516, 530
- Klypin, A., Kravtsov, A. V., Bullock, J. S., & Primack, J. R. 2001, *ApJ*, 554, 903
- Kravtsov, A. V., Berlind, A. A., Wechsler, R. H., Klypin, A. A., Gottlöber, S., Allgood, B., & Primack, J. R. 2004a, *ApJ*, 609, 35
- Kravtsov, A. V., Gnedin, O. Y., & Klypin, A. A. 2004b, *ApJ*, 609, 482
- Lacey, C. & Cole, S. 1993, *MNRAS*, 262, 627
- 1994, *MNRAS*, 271, 676
- Lahav, O., Lilje, P. B., Primack, J. R., & Rees, M. J. 1991, *MNRAS*, 251, 128
- Lokas, E. L. & Mamon, G. A. 2001, *MNRAS*, 321, 155
- Maller, A. H., Dekel, A., & Somerville, R. 2002, *MNRAS*, 329, 423
- Moore, B., Ghigna, S., Governato, F., Lake, G., Quinn, T., Stadel, J., & Tozzi, P. 1999, *ApJL*, 524, L19
- Moore, B., Katz, N., & Lake, G. 1996, *ApJ*, 457, 455
- Navarro, J. F., Frenk, C. S., & White, S. D. M. 1995, *MNRAS*, 275, 720
- 1996, *ApJ*, 462, 563
- 1997, *ApJ*, 490, 493
- Navarro, J. F., Hayashi, E., Power, C., Jenkins, A. R., Frenk, C. S., White, S. D. M., Springel, V., Stadel, J., & Quinn, T. R. 2004, *MNRAS*, 349, 1039
- Okamoto, T. & Habe, A. 1999, *ApJ*, 516, 591
- Paz, D. J., Lambas, D. G., Padilla, N., & Merchan, M. 2005, *astro-ph/0509062*
- Peebles, P. J. E. 1969, *ApJ*, 155, 393
- 1980, *The large-scale structure of the universe* (Research supported by the National Science Foundation. Princeton, N.J., Princeton University Press, 1980. 435 p.)
- Peirani, S., Mohayaee, R., & de Freitas Pacheco, J. A. 2004, *MNRAS*, 348, 921
- Plionis, M. & Basilakos, S. 2002, *MNRAS*, 329, L47
- Power, C., Navarro, J. F., Jenkins, A., Frenk, C. S., White, S. D. M., Springel, V., Stadel, J., & Quinn, T. 2003, *MNRAS*, 338, 14
- Press, W. & Schechter, P. 1974, *ApJ*, 187, 452
- Reed, D., Governato, F., Quinn, T., Gardner, J., Stadel, J., & Lake, G. 2005a, *MNRAS*, 359, 1537
- 2005b, *MNRAS*, 359, 1537
- Schechter, P. 1976, *ApJ*, 203, 297
- Shaw, L., Weller, J., Ostriker, J. P., & Bode, P. 2006, *ArXiv Astrophysics e-prints*
- Sheth, R. K. & Tormen, G. 2004, *MNRAS*, 350, 1385
- Springel, V. 2005, *MNRAS*, 364, 1105
- Springel, V., White, S. D. M., Jenkins, A., Frenk, C. S., Yoshida, N., Gao, L., Navarro, J., Thacker, R., Croton, D., Helly, J., Peacock, J. A., Cole, S., Thomas, P., Couchman, H., Evrard, A., Colberg, J., & Pearce, F. 2005, *Nature*, 435, 629
- Springel, V., White, S. D. M., Tormen, G., & Kauffmann, G. 2001, *MNRAS*, 328, 726
- Stadel, J., Katz, N., Weinberg, D. H., & Hernquist, L. 1997, [www-hpcc.astro.washington.edu/tools/skid.html](http://www-hpcc.astro.washington.edu/tools/skid.html)
- Summers, F. J., Davis, M., & Evrard, A. E. 1995, *ApJ*, 454, 1
- Tasitsiomi, A., Kravtsov, A. V., Gottlöber, S., & Klypin, A. A. 2004, *ApJ*, 607, 125
- Taylor, J. E. & Babul, A. 2004, *MNRAS*, 348, 811
- Tormen, G. 1997, *MNRAS*, 290, 411
- Tormen, G., Moscardini, L., & Yoshida, N. 2004, *MNRAS*, 350, 1397
- Tremaine, S. & Weinberg, M. D. 1984, *MNRAS*, 209, 729
- van den Bosch, F. C. 1998, *ApJ*, 507, 601
- van den Bosch, F. C., Abel, T., Croft, R. A. C., Hernquist, L., & White, S. D. M. 2002, *ApJ*, 576, 21
- van den Bosch, F. C., Tormen, G., & Giocoli, C. 2005, *MNRAS*, 359, 1029
- van Kampen, E. 1995, *MNRAS*, 273, 295
- Vitvitska, M., Klypin, A. A., Kravtsov, A. V., Wechsler, R. H., Primack, J. R., & Bullock, J. S. 2002, *ApJ*, 581, 799
- Wambsganss, J., Bode, P., & Ostriker, J. P. 2004, *Ap. J. Lett.*, 606, L93
- Warren, M., Quinn, P., Salmon, J., & Zurek, W. 1992, *ApJ*, 399, 405
- Wechsler, R. H., Bullock, J. S., Primack, J. R., Kravtsov, A. V., & Dekel, A. 2002, *ApJ*, 568, 52
- Weller, J., Ostriker, J. P., Bode, P., & Shaw, L. 2005, *MNRAS*, 944
- White, S. D. M. 1976, *MNRAS*, 177, 717
- 1984, *ApJ*, 286, 38
- Zentner, A. R., Berlind, A. A., Bullock, J. S., Kravtsov, A. V., & Wechsler, R. H. 2005, *ApJ*, 624, 505
- Zhao, D. H., Mo, H. J., Jing, Y. P., & Börner, G. 2003, *MNRAS*, 339, 12
- Zhao, H. 2004, *MNRAS*, 351, 891